Neuron

Article

Hierarchical Representations of Aggression in a Hypothalamic-Midbrain Circuit

Graphical Abstract

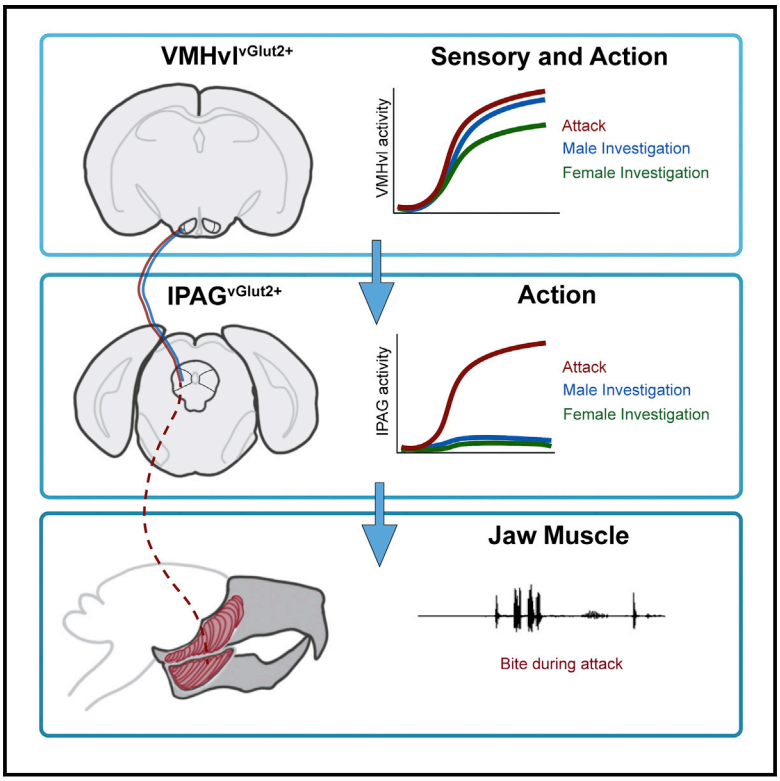

Highlights

- VMHvl^{vGlut2} neurons target IPAG^{vGlut2} neurons that project polysynaptically to the jaw
- Inactivating IPAG^{vGlut2} neurons results in aggressive action-specific deficits
- Single-unit IPAG activity is action specific and time locked to EMG-detected biting
- VMHvl-IPAG projection relays male-biased signals to generate action selectivity

Authors

Annegret L. Falkner, Dongyu Wei, Anjeli Song, ..., Patricia Chen, James E. Feng, Dayu Lin

Correspondence

afalkner@princeton.edu

In Brief

Although stimulation of the hypothalamus has long been known to evoke attack, how these neurons organize aggressive action is unknown. Here, Falkner et al. describe an excitatory hypothalamic-midbrain circuit that transforms generalized social information into an action-specific neural code that is time locked to the bite during attack.

Falkner et al., 2020, Neuron *106*, 637–648
May 20, 2020
https://doi.org/10.1016/j.neuron.2020.02.014

CellPress

Neuron

CellPress

Article

Hierarchical Representations of Aggression in a Hypothalamic-Midbrain Circuit

Annegret L. Falkner,[1,2,6,*] Dongyu Wei,[2] Anjeli Song,[3] Li W. Watsek,[2] Irene Chen,[2] Patricia Chen,[1] James E. Feng,[2] and Dayu Lin[2,4,5]

[1]Princeton Neuroscience Institute, Princeton, NJ 08540, USA
[2]Neuroscience Institute, New York University School of Medicine, New York, NY 10016, USA
[3]Boston University School of Medicine, Boston, MA 02118, USA
[4]Department of Psychiatry, New York University School of Medicine, New York, NY 10016, USA
[5]Center for Neural Science, New York University, New York, NY 10003, USA
[6]Lead Contact
*Correspondence: afalkner@princeton.edu
https://doi.org/10.1016/j.neuron.2020.02.014

SUMMARY

Although the ventromedial hypothalamus ventrolateral area (VMHvl) is now well established as a critical locus for the generation of conspecific aggression, its role is complex, with neurons responding during multiple phases of social interactions with both males and females. It has been previously unclear how the brain uses this complex multidimensional signal and coordinates a discrete action: the attack. Here, we find a hypothalamic-midbrain circuit that represents hierarchically organized social signals during aggression. Optogenetic-assisted circuit mapping reveals a preferential projection from VMHvl^{vGlut2} to lPAG^{vGlut2} cells, and inactivation of downstream lPAG^{vGlut2} populations results in aggression-specific deficits. lPAG neurons are selective for attack action and exhibit short-latency, time-locked spiking relative to the activity of jaw muscles during biting. Last, we find that this projection conveys male-biased signals from the VMHvl to downstream lPAG^{vGlut2} neurons that are sensitive to features of ongoing activity, suggesting that action selectivity is generated by a combination of pre- and postsynaptic mechanisms.

INTRODUCTION

The ventromedial hypothalamus ventrolateral area (VMHvl) has recently emerged as a critical hub for the integration of socially relevant information, exhibiting heterogeneous activity during the sensory, motor, and motivational phases of aggression. Neurons in this small excitatory subregion of the hypothalamus not only respond during attack itself but also show increased activity during sensory investigation of males and females and during the preparatory phase prior to attack (Falkner et al., 2016, 2014; Remedios et al., 2017; Lin et al., 2011; Hashikawa et al., 2017). In addition, suppression of VMHvl activity can have complex effects, decreasing not only the frequency of attack but also investigatory, sexual, and aggression-seeking behaviors (Yang et al., 2013; Lee et al., 2014; Falkner et al., 2016). How do neurons downstream of the VMHvl interpret this complex code to drive attack?

Outside of the hypothalamus, the periaqueductal gray receives the most prominent input from the VMHvl (Lo et al., 2019), and this area has long been known to play a role in expression of various survival behaviors. The emerging role of the periaqueductal gray (PAG) in expression of non-aggressive survival behaviors, such as stimulus-induced flight, appears to be that of a split-second action coordinator (Evans et al., 2018; Wang et al., 2019). We reasoned that a parallel circuit in the PAG might perform a similar function during conspecific attack.

In support of this, many decades of work across multiple species have firmly established a functional role of the PAG within the canonical "aggression circuit." Stimulation experiments in cats and rats first demonstrated that electrical stimulation of the PAG was able to evoke elements of defensive aggression (Fernandez De Molina and Hunsperger 1962; Mos et al., 1982; Gregg and Siegel, 2001), and that the effect of simulation can be facilitated through activation of glutamatergic synapses in the PAG (Siegel et al., 1997). Destruction of this area through aspiration or pharmacological means has been shown to dampen the behavioral effects of "upstream" stimulation, strongly indicating its role in the organization of aggressive action (Zalcman and Siegel 2006; Gregg and Siegel, 2003; Schreiner and Kling, 1953). Finally, a single paper reporting *in vivo* recordings in the PAG of cats shows a small number of neurons increasing during the coordinated attack response (Adams 1968). Although the functional role of the PAG in the aggression circuit has been firmly established, systems-level understanding of how this action coordination occurs in the circuit has been lacking.

The PAG is traditionally subdivided into columns that are molecularly and anatomically conserved across species (Bandler and Shipley, 1994; Bandler and Keay, 1996) and have distinct roles in coordination of survival behavior. Here we focused on the lateral PAG (lPAG) based on two criteria. First, this area is known to receive the densest projections from the VMHvl (Shimogawa

et al., 2015); second, previous studies have observed a high amount of immediate early gene expression following aggression (Lin et al., 2011). However, patterns of immediate early gene activation lack the temporal resolution to understand the precise interactions between the VMHvl and the PAG, and we do not yet understand the relationship between this putative action coordination area and its effectors. In this study, we use a combination of *in vivo* and *ex vivo* physiology, cell-type-specific perturbation, and multi-site optical recordings to explore how this hypothalamus-midbrain circuit coordinates aggressive action.

RESULTS

Because the PAG is a complex structure with several molecularly and anatomically distinct subregions that are known to receive hypothalamic input (Silva and McNaughton 2019), our first goal was to identify and map a functionally connected circuit using optogenetics-assisted circuit mapping. First we explored whether excitatory projection neurons from the VMHvl form functional connections with neurons in the lPAG. We targeted excitatory projection neurons by injecting a red-shifted cre-dependent excitatory opsin (AAV2.Syn.Flex.ChrimsonR.tdTomato) into the VMHvl of excitatory neurons (vGlut2-ires-cre mice) crossed with an Ai6 reporter (Figures 1A and 1B). We first confirmed that brief light pulses at the VMHvl were sufficient to reliably evoke action potentials (Figure 1C). Then we made coronal slices of the lPAG and performed voltage clamp recording from putative vGlut2+ and vGlut2− neurons (Figures 1D and 1E). We found that 50% (29 of 58) of identified vGlut2+ neurons exhibited short-latency excitatory postsynaptic currents (EPSCs) upon light delivery, whereas no single vGlut2− neurons (n = 12) exhibited this excitatory response (Figures 1F and 1G). Bath application of tetrodotoxin (TTX) and 4-aminopyridine (4-AP) did not change the magnitude of light-evoked EPSCs, supporting the monosynaptic nature of the connection (Figures 1H and 1I). None of the recorded cells showed inhibitory postsynaptic currents (IPSCs) upon light delivery.

We next hypothesized that a neural circuit that transforms a heterogeneous hypothalamic neural code into action would be linked to relevant musculature in as few synapses as possible. As a proxy for the implementation of aggressive action in mice, we focused on a single important effector for aggression: the jaw. By using intramuscular injections of a retrogradely transported pseudorabies virus (PRV) (Smith et al., 2000), neurons in the PAG have been previously identified as having polysynaptic projections to jaw muscles, critical for aggressive behavior (Fay and Norgren 1997). We injected the superficial masseter muscle of the jaw (a critical muscle for jaw closure) with GFP-labeled PRV 152 and confirmed that the majority of labeled neurons were located in the lPAG (Figure S1). We found that PRV-labeled neurons in the lPAG were overwhelmingly glutamatergic (Figures 1J and 1K). Using an Ai6 reporter line in combination with injections of a red-shifted PRV (PRV 614) in the jaw, we found that 297 of 327 red-labeled PRV-labeled neurons (90.8%) were labeled with GFP, indicating that these neurons are almost entirely excitatory (Figure 1K).

Next, we tested whether this effector-projecting subpopulation in the lPAG receives functional input from excitatory neurons from the VMHvl. Three weeks after injecting the VMHvl of vGlut2 × Ai6 mice with Chrimson, we injected the jaw with red-shifted PRV 614 (Figure 1L). Following PRV injections, animals were sacrificed animals 96 hours post injection, and lPAG slices were then prepared and recorded. We could evoke reliable EPSCs in slightly more than half of PRV+/vGlut2+ postsynaptic neurons in the lPAG (Figures 1M and 1N) by stimulating the excitatory projection from the VMHvl. Intriguingly, the failure rate in our ability to evoke EPSCs following a single 1-ms pulse of light was non-zero, indicating that this input could not reliably drive activity in the jaw-projecting lPAG neurons (Figure 1N, right). Overall, these data demonstrate a strongly preferential excitatory-to-excitatory circuit from glutamatergic hypothalamic neurons in the VMHvl to glutamatergic neurons in the lPAG, a subset of which project polysynaptically to aggression-relevant musculature.

We next tested the functional efficacy of this hypothalamic-midbrain projection. Attack of a castrated male has can be reliably evoked through stimulation of VMHvl cell bodies (Lin et al., 2011; Lee et al., 2014). We tested whether optogenetic activation of the VMHvl-PAG pathway could also reliably evoke attack. In some animals, we observed an upregulation of attack probability toward castrated males through this manipulation, but the ability to evoke attack was generally unreliable (Figure S2). Together, these data lend support to the hypothesis that the lPAG may organize specific motor aspects of attack but may not be sufficient to generate the full suite of attack behaviors in a reliable manner, similar to the VMHvl.

Chemogenetic Inactivation of PAG^{vGlut2} Leads to Aggression-Specific Deficits

Although inactivation of the VMHvl can result in a mixture of socially specific deficits (Yang et al., 2013; Lee et al., 2014; Falkner et al., 2016), we reasoned that, if the lPAG was involved in translating VMHvl signals into an aggression motor-specific code, then the effects may be action specific. To test this, we injected the lPAG of vGlut2-ires-cre males bilaterally with a cre-dependent genetically modified inhibitory receptor (AAV2-hSyn-DIO-hM4Di-mCherry) that silences neurons when activated by the synthetic ligand clozipine N-oxide (CNO). We tested whether inactivation of these neurons affected the expression of social and nonsocial behaviors following CNO or saline injection (Figures 2A and 2B). Here we found that inactivation of lPAG^{vGlut2} neurons following intraperitoneal (i.p.) CNO injection resulted in aggression-specific deficits relative to saline injection (Figures 2C–2F). Following CNO injections, mice spent less time attacking during interactions with males (Figure 2C; Video S1), and this was entirely due to a reduction in the duration of attack episodes (Figure 2D) rather than an increase in attack latency or a decrease in the number of attack episodes (Figures 2E and 2F). In contrast to attack, inactivation of the lPAG did not significantly affect the time spent investigating either males or females or the time engaged in sexual behaviors, as quantified by the time spent mounting the female (Figures 2G–2I). We observed no significant differences in alternate measure of these behaviors, including mean behavior duration, latency, or number of episodes. We found no difference between saline- and CNO-injected animals in the latency to approach and consume palatable food (Figure 2J), indicating that other behaviors requiring jaw closure were not affected.

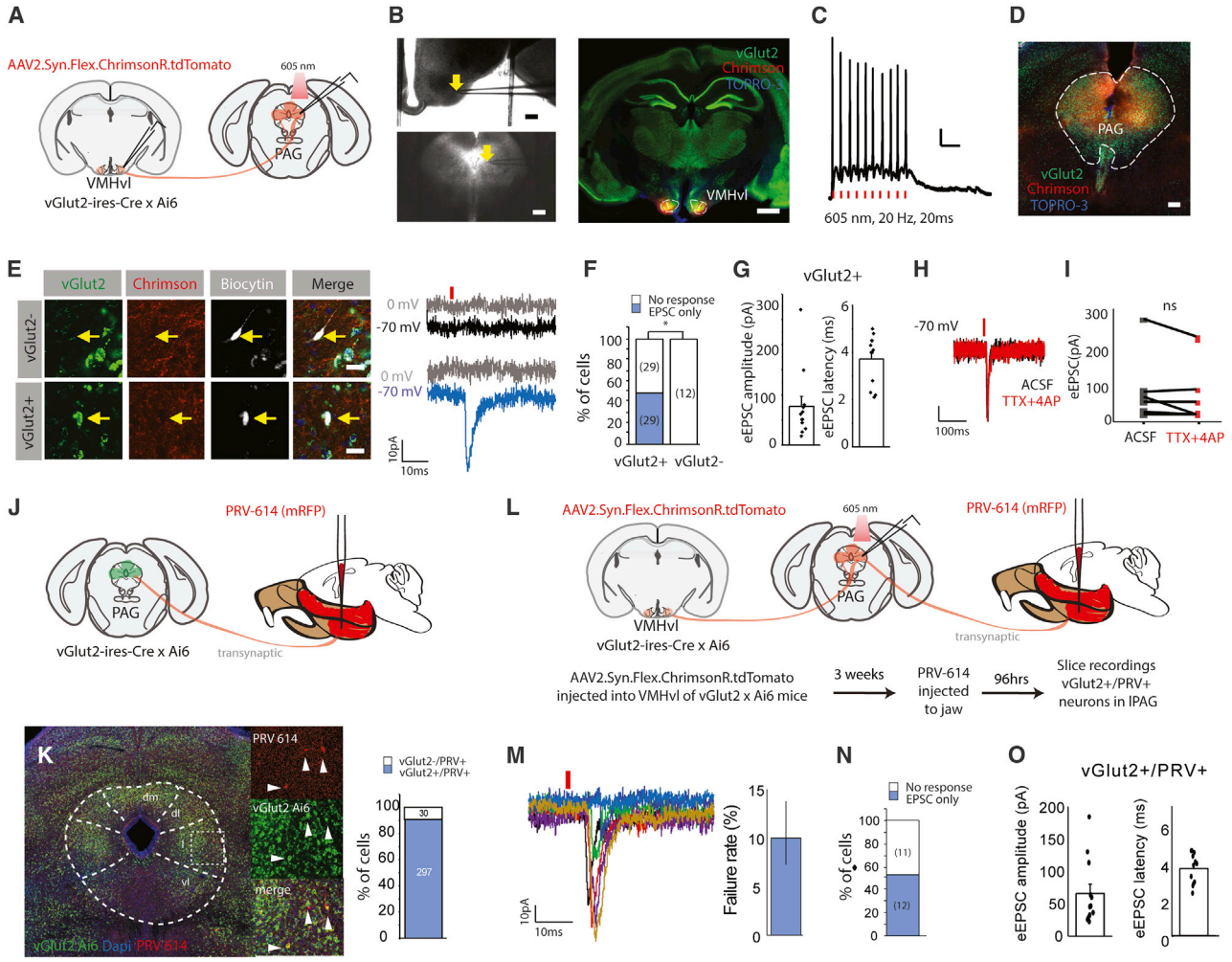

Figure 1. An Excitatory Circuit Connects the VMHvl to Jaw-Projecting Neurons in the lPAG

(A) Viral strategy for targeting excitatory projections from the VMHvl to the lPAG. Slices were made of VMHvl and lPAG, and whole-cell recordings were performed.

(B) Representative infrared differential interface contrast image (IR-DIC) from a recorded slice containing VMHvl (top left) and lPAG (bottom left). Yellow arrows indicate locations of recording pipette tips. Scale bars, 500 μm. Right: coronal section showing expression of Chrimson-tdTomato (red) from a vGlut2 × Ai6 mouse. Scale bar, 1 mm.

(C) Example trace showing current clamp recording of a VMHvl^{vGlut2} neuron expressing Chrimson-tdTomato. Presentation of 605-nm light pulses (20 Hz, 20 ms for 500 ms, red ticks) reliably evoked time-locked spiking. Scale bars, 100 ms (horizontal) and 10 mV (vertical).

(D) Histological image showing distribution of glutamatergic cells (green) and Chrimson-tdTomato-expressing fibers from the VMHvl (red) in the PAG. Blue: Topro-3. Scale bar, 200 μm.

(E) Enlarged views from (D) showing biocytin-filled vGlut2− (top row) and vGlut2+ cells (bottom row) and their corresponding recording traces showing 1 ms 605-nm light-evoked EPSC (−70 mV) and IPSC (0 mV). Yellow arrows indicate the locations of biocytin-filled cells. Scale bar (left), 20 μm; scale bars (right), 10 ms (horizontal) and 10 pA (vertical).

(F) Stacked bar graphs showing the percentage of recorded PAG cells receiving EPSC during light stimulation. Two-tailed Fisher's test, *p = 0.0132.

(G) Light-evoked EPSC amplitude (left) and latency (right) in PAG glutamatergic neurons (n = 12). Error bars show mean ± SEM.

(H) Example traces showing 1 ms 605-nm light-evoked EPSC before (black) and after 1 μM TTX and 100 μM 4-AP perfusion (red) in PAG glutamatergic neurons. Scale bars, 100 ms (horizontal) and 10 pA (vertical).

(I) No change in light-evoked EPSC amplitude before and after 1 μM TTX and 100 μM 4-AP perfusion in PAG glutamatergic neurons (n = 6). Paired t test, p > 0.05.

(J) Schematic describing the strategy for quantifying jaw-projecting lPAG$^{vGlut2+}$ neurons.

(K) 297 of 327 (90.8%) PRV 614-labeled neurons in lPAG were vGlut2-Ai6+ (example overlap shown in K, bottom right).

(L) Strategy for functional targeting of jaw-projecting lPAG neurons.

(M) Example traces showing 1 ms 605-nm light-evoked EPSC in one PAG^{vGlut2} neuron. Scale bars, 10 ms (horizontal) and 10 pA (vertical).

(N) Summary (left; n = 27 cells, N = 8 mice) and failure rate (right) and stacked bar graph showing that 12 of 23 PAG PRV+ vGlut2+ neurons received glutamatergic input from VMHvl.

(O) Light-evoked EPSC amplitude and latency in PAG PRV+ vGlut2+ neurons (n = 23). Error bars show mean ± SEM.

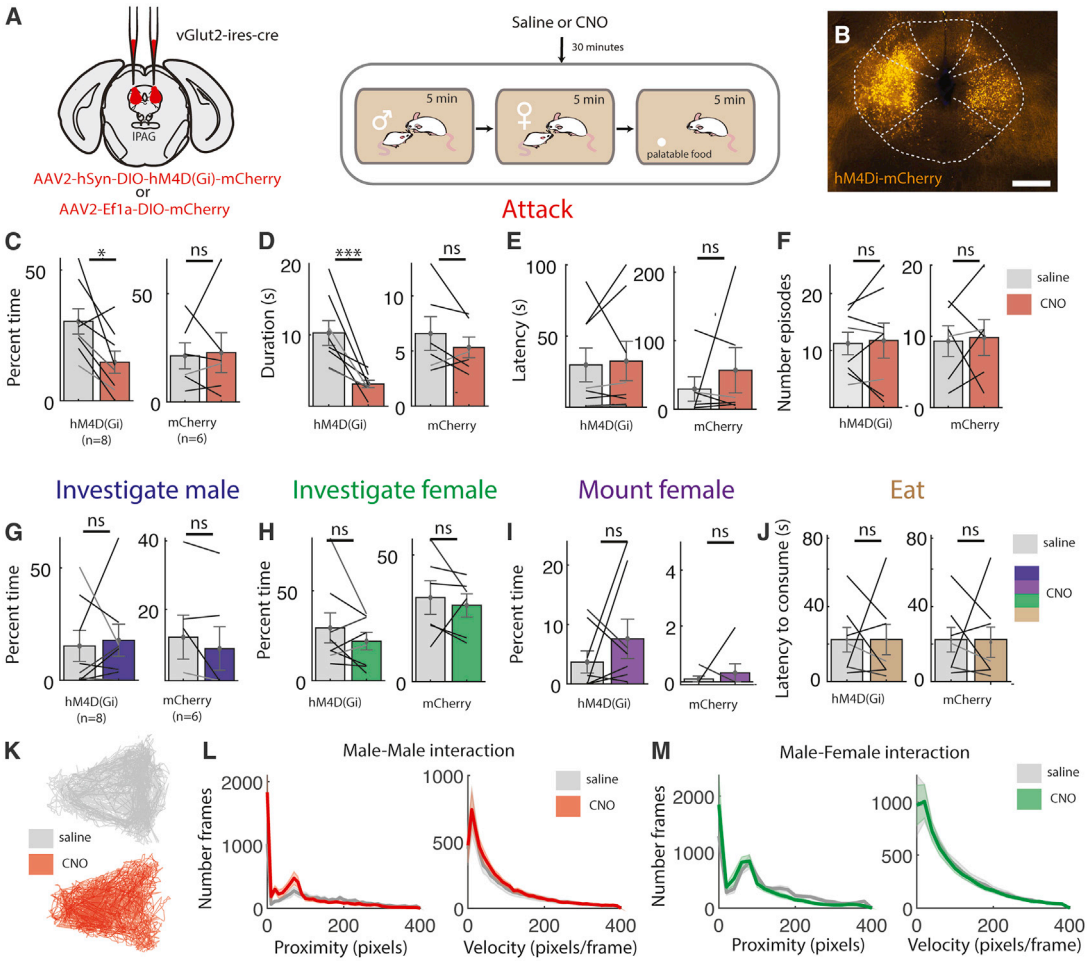

Figure 2. Chemogenetic Inactivation of lPAG Results in Aggression-Specific Deficits

(A) Viral strategy for reversible inactivation of lPAG. vGlut2-ires-cre animals were injected bilaterally with DIO-hM4D(Gi)-mCherry (N = 8 animals) or DIO-mCherry (N = 6 animals). After injection with either saline or CNO, animals were tested during interactions with males and females and then given access to palatable food.

(B) Example histology showing expression of hM4Di-mCherry in the PAG. Scale bar, 500 μm.

(C–F) Following CNO-mediated inactivation in hM4Di-injected animals (left panels), the percentage of time spent attacking was reduced relative to saline (C, p = 0.016). This effect was entirely due to reduced attack duration following inactivation (D, p = 0.004) and not changes in attack latency (E, p = 0.784) or the number of attack episodes (F, p = 0.772). No effects on attack were observed in control animals (right panels, C–F; p = 0.854, p = 0.236, p = 0.480, p = 0.854).

(G–J) In contrast to attack, no effects on other social or jaw-dependent behaviors were observed. CNO inactivation did not affect the percentage of time spent investigating males (G; hM4Di, p = 0.751; mCherry, p = 0.239), time spent investigating females (H; hM4Di, p = 0.270; mCherry, p = 0.584), mounting females (I; hM4Di, p = 0.332; mCherry, p = 0.567), or latency to approach and consume a yogurt pellet (J; hM4Di, p = 0.998; mCherry, p = 0.998); paired t tests.

(K–M) We tracked the locations of saline- and CNO-injected animals (K) during male-male (L) and male-female (M) interactions. No significant differences in the distribution of inter-animal distance (L and M, left; p = 0.243, p = 0.154) or velocity (L and M, right; p = 0.999, 0.999) were observed between saline and CNO injection.

We used machine-vision tracking (DeepLabCut; Mathis et al., 2018) to quantify the inter-animal proximity and movement velocity during interactions following saline and CNO administration (Figure 2K). We found no significant difference in the overall distribution of inter-animal proximity or resident velocity in either male-male (Figure 2L) or male-female interactions (Figure 2M), indicating that inactivation of lPAG^{vGlut2} did not result in non-specific motor or motivational deficits. Together, these cell-type-specific inactivation data suggest a specific role of lPAG^{vGlut2} in the execution and maintained coordination of attack.

PAG Neurons Encode a Simplified Action-Selective Code Relative to VMHvl

The aggression-specific deficit observed during lPAG inactivation indicates that the PAG's role within the aggression circuit is uniquely action selective. To confirm this, we recorded populations of single neurons in the lPAG during free social interactions and compared the response profiles with newly quantified measures of previously recorded neurons from the VMHvl (Falkner et al., 2014; Lin et al., 2011). Electrode tracks in all animals were confirmed to be located in the lPAG post hoc using a fluorescent lipophilic dye (Figure 3A). We examined the firing rates of

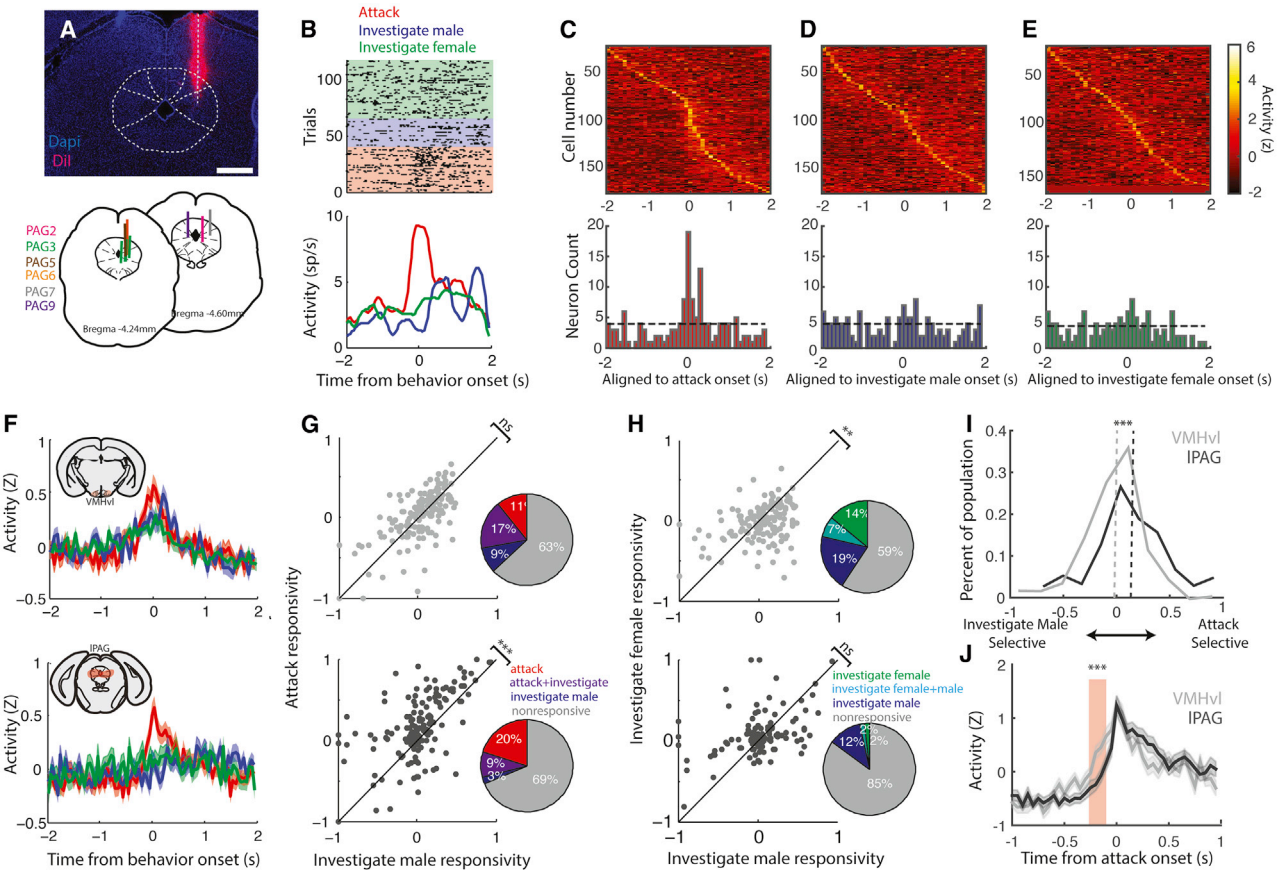

Figure 3. Activity in the lPAG Is More Attack Selective Than in the VMHvl

We performed chronic single-unit recordings in the lPAG during social behaviors and compared these responses with activity in the VMHvl.

(A) Histology showing example placement of electrode bundles (and one group of tetrodes [PAG3]) in the lPAG and electrode track locations for all recording animals (N = 6). Scale bar, 1 mm.

(B) Example raster plot (top) and peri-event time histogram (bottom) for activity of an example lPAG unit aligned to attack (red), investigation of a male (blue), and investigation of a female (green), sorted by behavior.

(C–E) Normalized responses of a population (top) of recorded neurons, sorted by peak of response aligned to attack (C; N = 159), investigation of males (D; N = 158), and investigation of females (E; N = 151). Bottom: histograms showing the number of units with a response peak above 95% confidence interval (CI) in each bin. Dotted black lines (C–E) represent chance levels for each behavior.

(F) Normalized population response, mean ± SEM, of VMHvl (top) and lPAG (bottom) during onset of key behaviors during interactions with males (attack [red] and investigation of males [blue]) and females (investigation of females [green]) (N = 166,156 for VMHvl male attack and investigation, N = 212 for female investigation, N = 159 for lPAG male attack and investigation, N = 151 for female investigation).

(G and H) Comparison of responsivity of individual VMHvl neurons (G and H, top, light gray) and lPAG neurons (G and H, bottom, dark gray). The VMHvl population is nonselective between attack and investigation of males (G, top; p = 0.806, N = 157) and selective for investigation of males compared with females (H, top; p = 0.005, N = 147), whereas lPAG is selective for attack relative to investigation of males (G, bottom; $p = 3.4 \times 10^{-7}$, N = 152) and nonselective for investigation of males and females (H, bottom; p = 0.415, N = 152). Tests in (G) and (H) were performed using Wilcoxon signed-rank test. Pie chart insets displaying percentages of individually significant neurons (Bonferroni-corrected t test) in VMHvl and lPAG show an increasing number of purely attack-selective neurons in the lPAG relative to the VMHvl and a decrease in investigation-selective neurons in the lPAG.

(I) Selectivity of population to attack compared with selectivity to investigate male shows the attack-shifted peak for the lPAG population (dark gray) relative to VMHvl (light gray), shown using the responsivity index (RI) value. p = 0.0001, Kolmogorov-Smirnov test.

(J) Attack-responsive neurons in the VMHvl (light gray) have significantly increased activity prior to attack onset relative to attack-responsive lPAG neurons (dark gray). N = 44 neurons in the VMHvl, N = 46 neurons in the lPAG, p = 0.0005, Bonferroni-corrected unpaired t test across all bins.

single units aligned to attack, investigation of males, and investigation of females (Figures 3B–3E). Across the population (n = 164 neurons, 6 animals), we observed that a subpopulation of neurons in the lPAG exhibited their peak firing aligned to the onset of attack, whereas few neurons exhibited peak firing aligned to the onset of either investigation of male or female conspecifics (Figures 3C–3E).

This selectivity for attack differs substantially from the response properties of the VMHvl. The VMHvl exhibits distinct activity peaks aligned to attack, investigation of males, and investigation of females (Figure 3F, top). In contrast, the population response at the lPAG only reveals an increase during attack (Figure 1F, bottom). To compare the responses of single neurons in these populations, each neuron was assigned a responsivity

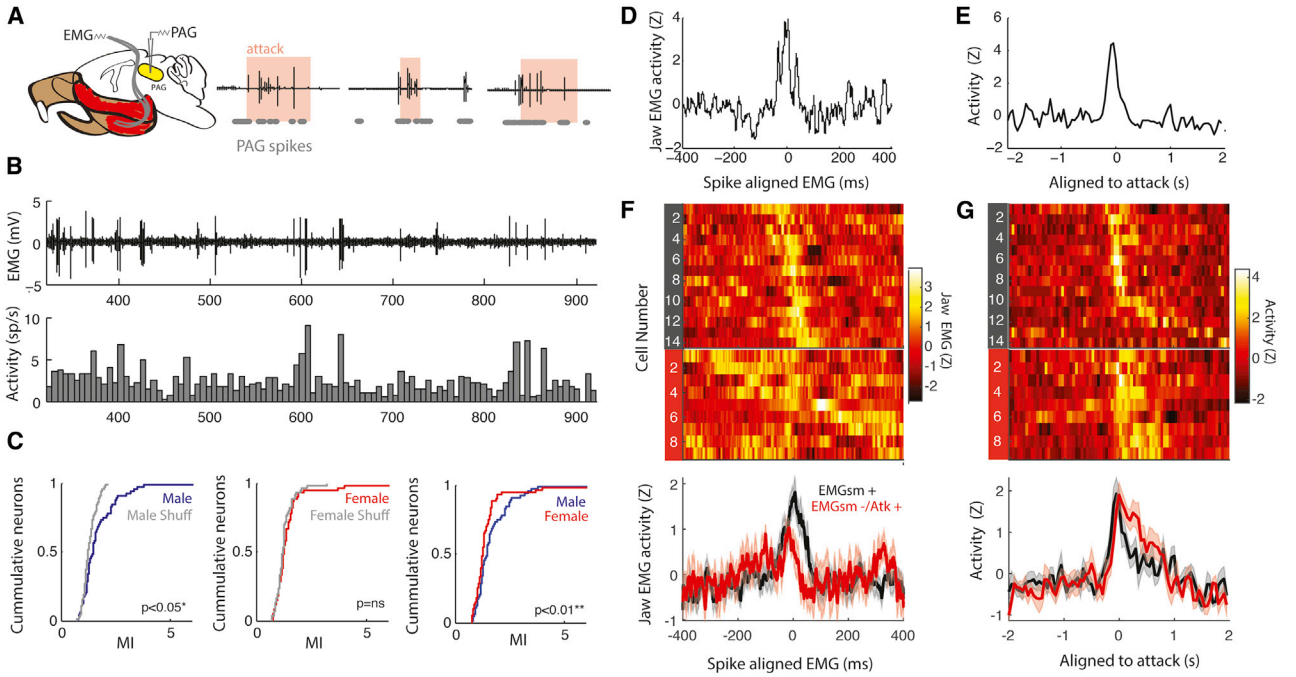

Figure 4. IPAG Spiking Has Precise Temporal Alignment with Jaw Muscle Activity during Aggression

(A) Example simultaneous recordings of jaw EMG and IPAG spiking during attack episodes, shown in red.

(B) Example EMG (top) and activity from simultaneously IPAG neuron (bottom) during interaction with a male.

(C) Mutual information (MI) of IPAG spiking and EMG activity, compared during interactions with males and females (N = 64 neurons); MI of activity during male interaction compared with the time-shuffled control ($p = 0.0214$, paired t test); MI of activity during female interactions compared with the time-shuffled control ($p = 0.1551$, paired t test); and MI of activity during male and female interactions ($p = 0.0053$, paired t test).

(D and E) Example STEMG (D) and attack-aligned PETH (E) with precise temporal alignment to EMG.

(F and G) STEMG (F) and attack-aligned activity (G) of neurons with significant STEMG (red, top trace) and significant attack-responsive neurons that do not have significant STEMG (black, bottom trace), showing distinct dynamics.

score for each behavior (relative to its response during nonsocial behaviors). We determined the number of Bonferroni-corrected, significant neurons for each behavior in both populations (Figures 3G and 3H). We found that the population of lPAG neurons is significantly more attack selective than investigation selective, whereas the VMHvl population has equal responsivity for both behaviors (Figure 3G). In addition, we found that lPAG exhibited an increased number of uniquely attack-responsive neurons and showed a decrease in co-selective and investigation-selective single units relative to the VMHvl (Figure 3G; $p = 0.0031$, chi-square test). Consistent with this, we also observed that the lPAG population shows little selectivity for either male or female investigation (Figure 3H; $p = 0.0210$). Overall, we found that the selectivity for attack was increased in the lPAG compared with the VMHvl and that the activity of attack-selective neurons in the VMHvl increased earlier than that of attack-selective neurons in the lPAG (Figures 3I and 3J).

lPAG Neurons Exhibit Time-Locked Activity to Jaw Muscle Activity

Given that a subpopulation of $lPAG^{vGlut2}$ receives excitatory input from the VMHvl and projects polysynaptically to the jaw, we hypothesized that neurons in the lPAG may have a specific role in coordinating attack-relevant musculature. We developed a preparation to simultaneously record from neurons in the lPAG and electromyography (EMG) activity from the superficial masseter (EMG_{SM}) while animals were attacking and performing other social interactions (Figures 4A and 4B; Video S2; n = 64 neurons in 4 animals). We used mutual information (MI) to quantify whether the EMG_{SM} signal provides useful information in predicting the activity during male or female interactions. MI provides a model-free method for capturing the amount of joint information between two signals, and increased MI indicates that one signal can be used to predict the other (Srivastava et al., 2017). We calculated MI for each neuron and associated EMG_{SM} signal relative to a circularly permuted time-shuffled control during interactions with males and females. We observed that, across the population of recorded neurons, EMG_{SM} increased the MI during male interactions but not during female sessions relative to the shuffled control and also that MI provided by the EMG_{SM} signal was significantly higher during male interactions compared with female interactions (Figure 4C), indicating that a subpopulation of neurons is modulated during attack-related jaw movement but not similarly activated by nonspecific jaw movements during female interactions.

We hypothesized that the activity of jaw-activated neurons might have a tight temporal relationship to the muscle activity when it is involved in directly activating the muscle. We examined

the relationship between individual spikes and the EMG_{SM} signal. For each neuron, we generated a spike-triggered EMG (STEMG) across an 800-ms bin around each spike and used strict criteria (5 consecutive points must lie above the 98% confidence interval) to determine whether each STEMG demonstrated a significant relationship with individual spikes (Davidson et al., 2007). We found that a subpopulation of recorded neurons (21.8%, 14 of 64 neurons) showed a significantly increased STEMG within 60 ms of spikes during interactions with males (EMG_{SM}+; Figures 4D and 4F). Most of these EMG_{SM}+ neurons (12 of 14) were activated during attack (EMG_{SM}+; Figures 4E and 4G). In contrast, neurons that were identified as being significantly activated during attack that were not overlapped with our EMG-identified subpopulation (EMG_{SM}−/Atk+) showed distinctly different activity profiles in the STEMG and during attack (EMG_{SM}−/Atk+). STEMG response profiles of EMG_{SM}−/Atk+ neurons were diverse but often exhibited suppression following PAG spiking (Figure 4F, black). Furthermore, the activity of these EMG_{SM}−/Atk+ neurons during attack showed that the responses were increased not just at the onset of attack but showed activation that persisted through the attack (Figure 4G, black). These data are consistent with the hypothesis that attack-related neurons in the lPAG may activate multiple attack-related muscles, including jaw opening musculature. A much smaller number of neurons (7.8%, 5 of 64 neurons) exhibited a time-locked relationship during female interactions, which suggests that a small minority of jaw-responsive neurons may be recruited during other (nonaggressive) behaviors.

We closely examined the activity of these same neurons recorded simultaneously with EMG during other jaw-related behaviors including eating and grooming (Figure S3). Although all three behaviors (attack, grooming, and eating) produced significantly increased activity of the rectified EMG and could be observed in single behavioral trials, we observed an increase in the activity of the neural population only following attack and not in the other EMG-detected behaviors, providing further support for the specificity of this population in coordinating jaw-related motor plans related to aggression.

Pathway-Specific Fiber Photometry Reveals a Male-Biased Signal in the VMHvl-PAG^{vGlut2} Projection

Our data demonstrate that neurons in the lPAG exhibit a greater degree of selectivity for aggressive action than the VMHvl. One simple mechanism by which this circuit could perform the transformation is if the projection from the VMHvl to PAG were a labeled line for either attack-specific or male-specific information. To explicitly test this, we targeted excitatory VMHvl-PAG-projecting neurons by injecting the ipsilateral side of a vGlut2-ires-cre male mice with a retrogradely transported herpes simplex virus, cre-dependent calcium indicator (HSV-Ef1a-LS1L-GCaMP6f) into the lPAG. On the contralateral side, we injected a cre-dependent calcium indicator (AAV1.CAG.-Flex.GCaMP6f.WPRE.SV40) in the VMHvl to compare the activity from the total VMHvl vGlut2+ population, not specified by projection. We positioned fibers over the ipsi- and contralateral VMHvl and used fiber photometry to simultaneously record from the VMHvl-PAG^{vGlut2} and VMHvl^{vGlut2} populations, respectively, during free social interactions (Figures 5A–5C).

We found that both VMHvl^{vGlut2} and VMHvl-PAG^{vGlut2} populations showed a strong bias toward male compared with female mean activity (Figure 5D). However, we observed that activity during male interaction was not significantly different (Figure 5E), whereas, during female interactions, VMHvl-PAG activation decreased relative to the overall VMHvl population response. In addition, to track how well the two signals match, we computed the correlation (Pearson r) between the simultaneously recorded activity of VMHvl^{vGlut2} and VMHvl-PAG^{vGlut2} populations during single behavior "trials" as animals were attacking or investigating males or females (Figures 5F and 5G). High correlations in these experiments indicate that VMHvl-PAG^{vGlut2} population sends a faithful copy of the VMHvl^{vGlut2} activity to the lPAG. We found that single-trial correlations during male behaviors were similar (Figure 5F, left). In contrast, correlations during investigation of females were significantly lower (Figure 5F, center and right), indicating that the population is male selective. Across all animals, we found that correlation coefficients during male interactions significantly increased during male interactions relative to female interactions (Figure 5G). Together, these data indicate that the VMHvl-PAG^{vGlut2} population behaves as a labeled line, selectively filtering activity during female interactions. We did not find evidence for an attack-specific labeled line (Figure 5F; Figure S4). To quantify this, we compared the PETHs of activity in the VMHvl$^{vGlut2+}$ population and the VMHvl-PAG$^{vGlut2+}$ projection during attack and investigation of males. Similar to the single-unit data, both VMHvl$^{vGlut2+}$ and VMHvl-PAG$^{vGlut2+}$ activity also showed clear peaks aligned with attack and investigation of males that were very strongly correlated during individual behavior episodes.

Together, these data demonstrate that an excitatory projection from the VMHvl to the lPAG conveys male-biased information to excitatory downstream populations, behaving as a labeled line for aggression-relevant information. Although this projection effectively filters female-evoked signals, it does not filter other male interactions, such as investigation. This suggests that further downstream mechanisms are needed to transform VMHvl activity to an aggression-specific signal motor code. One possibility is that the PAG is sensitive to specific temporal features in its inputs prior to attack-induced activation, including slower investigation-evoked increases that precede attack. To specifically test this, we performed simultaneous recordings of VMHvl$^{vGlut2+}$ and PAG^{vGlut2} (Figures 6A–6C) using multisite fiber photometry and computationally modeled the interactions between these two signals. Qualitatively, we observed that, during male interactions, PAG^{vGlut2} activity peaks often followed VMHvl^{vGlut2} activity peaks, whereas, during female interactions, signal dynamics were more independent (Figures 6B and 6C; Figures S4D–S4F). In support of this observation, we found that trial-to-trial comparison of the VMHvl$^{vGlut2+}$ and lPAG^{vGlut2} exhibited much higher correlations during attack than either investigation males or females (Figure 6D). These lower correlations during investigation behaviors demonstrate more uncoupled signals between the two brain areas.

To quantify the time dependence of the interactions between VMHvl$^{vGlut2+}$ and lPAG^{vGlut2} activity, we computed the cross-correlation of the simultaneously recorded signals separately

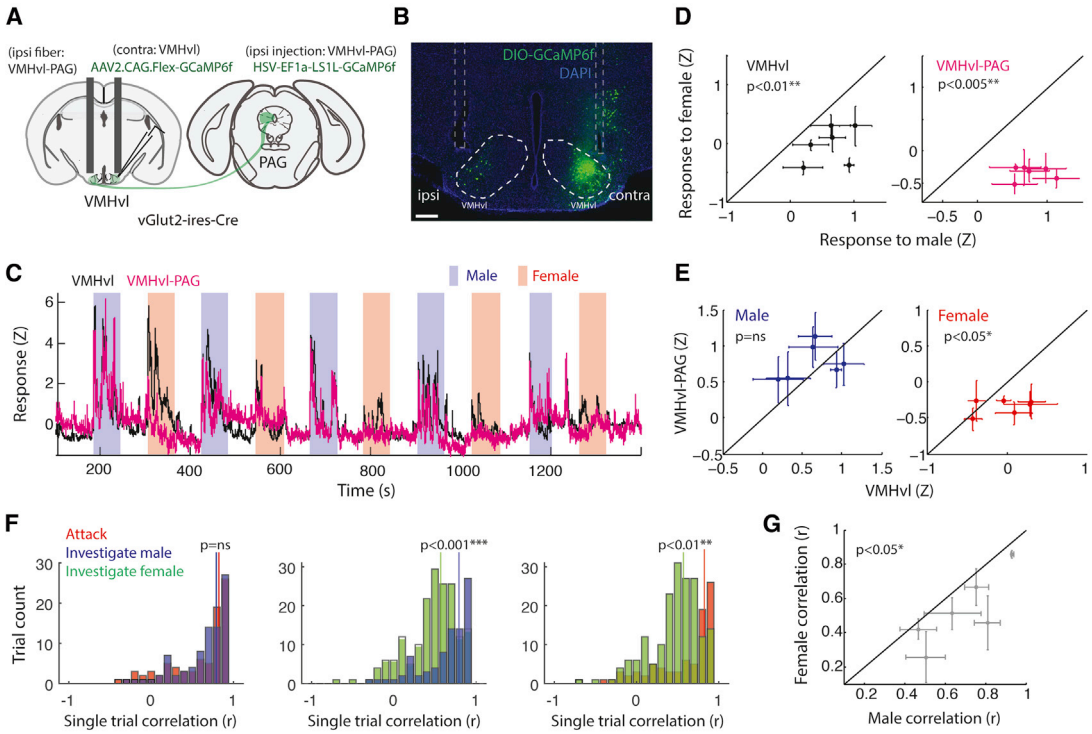

Figure 5. Activity in lPAG-Projecting VMHvl Neurons Conveys Preferentially Male-Specific Information

(A) Experimental configuration of bilateral injection of GCaMP6f into vGlut2-ires-Cre mice for simultaneous fiber photometry recordings of VMHvl and VMHvl-PAG projection neurons. The ipsilateral injection targets VMHvl^{vGlut2} neurons, and the contralateral injection targets VMHvl-PAG^{vGlut2} projection neurons.

(B) Example histology of GCaMP-labeled VMHvl^{vGlut2} neurons (right) and VMHvl-lPAG^{vGlut2} neurons (left) and placement of fiber tracks. Scale bar, 300 μm.

(C) Example simultaneous recording of VMHvl^{vGlut2} (black) and VMHvl-PAG^{vGlut2} (magenta) projection neurons during alternating interactions with males (blue) and females (red).

(D) Population activity (mean + SEM for each animal, N = 6 animals) of comparison between activity during male interaction and female interaction for VMHvl neurons (left, p = 0.0062) and VMHvl-PAG projection neurons (right, p = 0.0002), showing that both populations exhibit increased activity with males.

(E) Simultaneously recorded activity of VMHvl ^{vGlut2} and VMHvl-PAG ^{vGlut2} neurons is not significantly different during male interactions (left, p = 0.3676), but activity during female interaction is reduced in VMHvl-PAG neurons (right, p = 0.044).

(F) Distributions of the Pearson correlation between behavior-aligned activity in VMHvl and VMHvl-PAG. Correlation distributions are not significantly different between attack and investigation of males (left, p = 0.358, unpaired t test, N = 83 attack trials, N = 85 investigation of males trials), but correlations are higher in both attack and investigation of males than during investigation of females (center, p = 0.00002; right, p = 0.004; unpaired t test; N = 180 investigate female trials). Solid lines represent distribution medians.

(G) Correlation of simultaneously recorded VMHvl^{vGlut2} and VMHvl-PAG^{vGlut2} neurons is higher for male interactions than female interactions (p = 0.0238).

All tests (D, E, and G) used a paired t test.

for social behaviors and a baseline no-interaction epoch. We found that cross-correlation during male interactions was strongly and asymmetrically skewed across a multi-second timescale, indicating that increases in VMHvl signals "lead" PAG signals during interactions with males but not females (Figures 6E and 6F). The integral of the cross correlation during the "pre" epoch (VMHvl leads PAG) relative to the "post" epoch (PAG leads VMHvl) significantly increased during male interactions across the population of recorded animals (n = 7, p = 0.0174, paired t test) and was not significantly different during interactions with females or the no-interaction baseline period (p = 0.9333, p = 0.6148, paired t test).

The slow temporal dynamics of the cross-correlation during male interactions suggests that PAG activity is influenced by VMHvl activity stretching backward in time. To specifically quantify this temporal relationship between the VMHvl and lPAG, we modeled the ongoing PAG activity using a time-varying linear regression model (Figure 6G). We iteratively fit PAG activity with the activity of the VMHvl (VMHvl → lPAG) with a family of models with a variable number of regressors representing increasing numbers of previous time bins, used Akaike information criteria (AIC) to select the best model within each family, and cross-validated this model on a separate dataset for each recorded animal. We performed this model selection separately for male and female interactions and across a variety of bin sizes, ranging from 50 ms to 1 s. We found that cross-validated fits for the best fit model were significantly better during male but not female interactions relative to a time-shuffled control. Importantly, this effect was consistent across a range of bin sizes (Figure 6H), indicating that this variable made little difference in the model fit. In addition, we extracted the model order (number of time bins) for the best fit model for

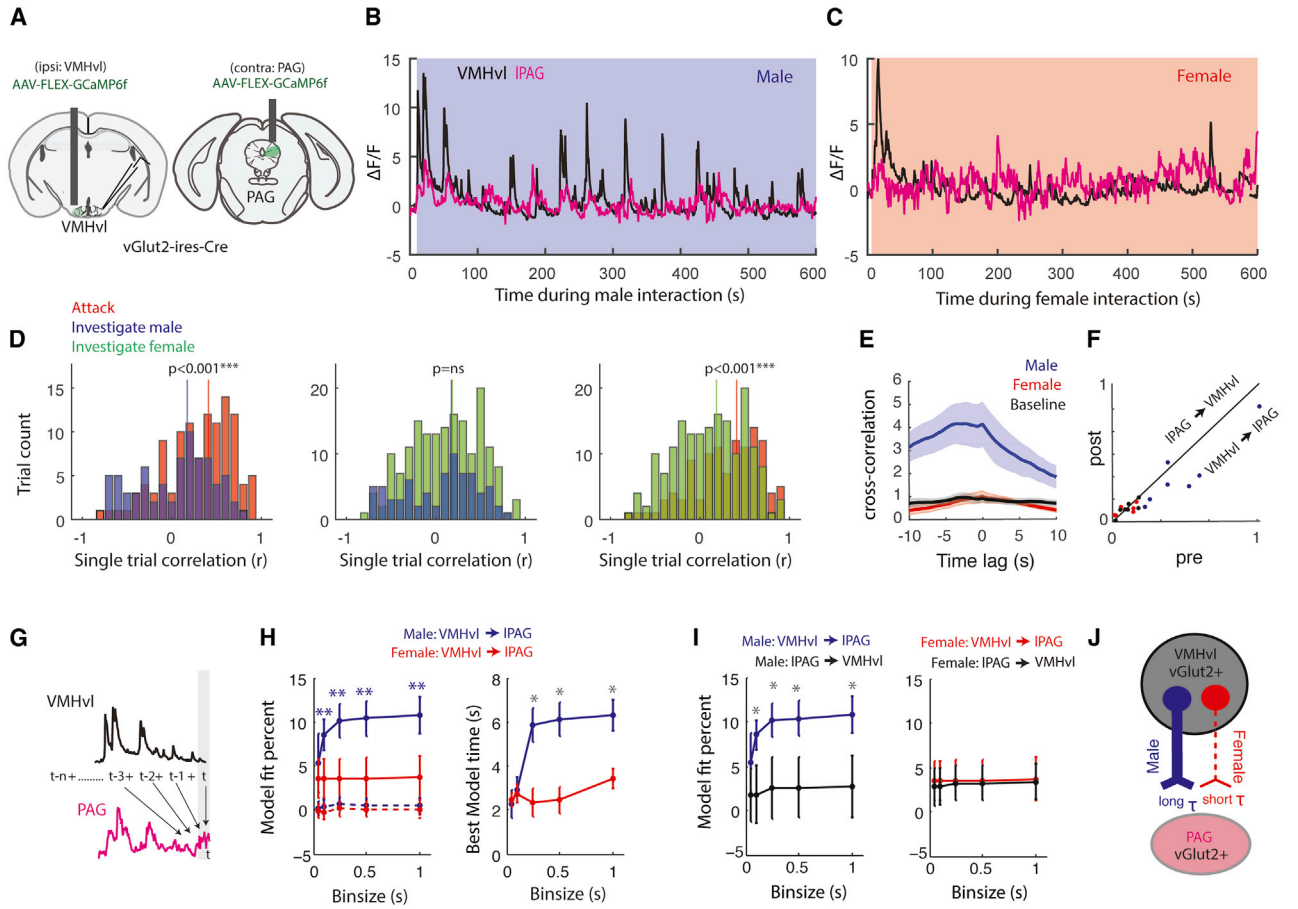

Figure 6. Simultaneous Recordings of VMHvl^{vGlut2} and lPAG^{vGlut2} Reveal that lPAG Activity Is Preferentially Coupled to the VMHvl during Attack and Preferentially Sensitive to VMHvl Activity History during Male Interactions

(A) Experimental configuration and viral strategy for simultaneous recordings during social interactions. Example recording of VMHvl^{vGlut2} and lPAG^{vGlut2} during interaction with a male (B) and female (C).

(D) Distributions of Pearson correlation between behavior-aligned activity in VMHvl ^{vGlut2} and lPAG ^{vGlut2}. Correlation distributions are significantly higher for attack than investigation of males or females (left, p = 0.00003, unpaired t test; right, p = 0.00006, N = 112 attack trials, N = 73 investigate male trials, N = 174 investigate female trials), but correlation distributions are similarly low for investigation of either males or females (center, p = 0.240). Solid lines represent distribution medians.

(E) Cross-correlation of simultaneously recorded signals during male interactions (blue), female interactions (red), and no-interaction baseline (black).

(F) Comparison of summed cross-correlation in the pre epoch (−10 s to 0 s) and post epoch (0 s to 10 s) for male, female, and no-interaction baseline shows significant asymmetry only during male interaction (N = 7 animals, male *p = 0.0174, female p = 0.9333, baseline p = 0.6148).

(G) PAG ^{vGlut2} activity was fit with a linear model using a variable amount of preceding VMHvl ^{vGlut2} signal as the regressor.

(H) Fit percent (center) and time (right) associated with best fit models of cross-validated data using a time-varying input from the VMHvl. Dotted lines represent data from time-shuffled controls.

(I) Controls for the time-varying regression model, comparison of forward (VMHvl → lPAG) and reverse (lPAG → VMHvl) regressive models, and model fit percentages for fits during male (left) and female (right) interactions. Black traces show reverse models. During male interactions (blue), fits are significantly increased in the forward model relative to the reverse model (*p < 0.05, paired t test for each time bin).

(J) Conceptual model of pathway selectivity of male-responsive information.

each animal for male and female interactions for each bin size. We found that the elapsed time associated with these best fit models was significantly longer for male interactions than female interactions (Figure 6H, right), indicating that, during male interactions, PAG signals are influenced by VMHvl signals stretching farther back in time.

On a conceptual level, this suggests that activity in the VMHvl increases prior to activation of the PAG, an effect that is consistent with the action specificity of the PAG and the fact that activity in the VMHvl appears to increase prior to lPAG (Figure 3J). To control for correlations driven purely by the signal kinetics of our calcium indicator, we also fit the reverse circuit model (lPAG→ VMHvl) and found that both the fits and model order are significantly decreased relative with the forward circuit model during male (Figure 6I). Together, these results suggest a model where, during interactions with males but not during interactions with females, the PAG receives VMHvl inputs conveying information about the sensory properties of the stimulus obtained during investigation, and

this information is integrated over several seconds to coordinate attack behavior (Figure 6J).

DISCUSSION

These findings provide the first direct evidence that the role of the lPAG in the aggression circuit is to transform the complex sensory-motor and motivational signals of the hypothalamus into aggressive action-specific code. Because neural signals are time locked to jaw movement during aggression, we propose that the role of the lPAG in aggression is to coordinate effector-specific musculature, including the jaw. We build on decades of elegant functional manipulation experiments to provide a systems-level description of the hierarchical representations of aggression in the hypothalamus and midbrain, with downstream lPAG neurons representing a "simplified" action-selective neural code relative to the VMHvl. These results add to growing literature that positions the PAG as a critical coordinator of survival actions that are determined by combinations of noisy sensory and state-dependent inputs (Koutsikou et al., 2017).

Because PAG neurons are active later and more acutely during attack behavior than its hypothalamic inputs from the VMHvl, it may serve as a behavioral initiation threshold, as suggested for other survival behaviors. We do not mean to suggest that the lPAG is "for" aggression; the PAG (and, in particular, hypothalamic-PAG pathways) have been implicated in many sensory-driven behaviors, including but not limited to threat responsivity (Wang et al., 2015; Evans et al., 2018), prey capture (Li et al., 2018), itch (Gao et al., 2019), oro-motor coordination (Stanek et al., 2014), and social avoidance following defeat (Franklin et al., 2017). Additionally, the PAG has a well-documented role across species in generation of vocalization, a behavior that also requires integration of social-sensory signals and coordination of facial and laryngeal musculature (Kittelberger et al., 2006; Holstege, 2014; Tschida et al., 2019). Here we add to this literature by characterizing the neural code during conspecific attack and further hypothesize that the PAG is capable of orchestrating many complex survival behaviors by coordinating output to relevant muscles through sex-selective processing of specific temporal features in its inputs (Fang et al., 2018).

How does this transformation occur? Here we show that the lPAG provides a functional link between excitatory activity in the VMHvl and a jaw-projecting excitatory population. This PAG-projecting VMHvl population is a partial labeled line, filtering out some aggression-irrelevant signals, but is not a "pure" action selective signal, implying that further downstream mechanisms are needed to generate the action-selective code. One simple hypothesis is that the PAG simply represents the accumulation bound from VMHvl input: when VMHvl activity is high, this drives activity in the PAG when a particular threshold is reached. Although simple and compelling, this does not account for the fact that, at the level of the VMHvl population, activity during male investigation and attack are indistinguishable, activity from both behaviors is relayed to the PAG, but the PAG is activated only during attack. A second possibility is that, if input is noisy, then high-fidelity spikes from the VMHvl occur only at or around initiation of attack, activating post-synaptic PAG neurons, similar to the effects observed in a circuit for defensive escape (Evans et al., 2018). We observed that the failure rate for the VMHvl-lPAG synapse here is relatively low (~10%; Figure 1). Although lower than the failure rate observed in the escape circuit (~30%), it is non-zero, indicating that spike fidelity may still play a role in driving this circuit.

Another possibility is that transformation to an action-selective code may occur at the local level within the lPAG. Mixed sensory and action signals may target a subpopulation of lPAG neurons that respond during both sensory and action phases of aggression, and then local attack-selective populations project to an effector-specific output lPAG population. A subpopulation of single neurons within that population responds to sensory variables, demonstrating significant response heterogeneity within this circuit (Figure 3G). Second, a subpopulation of these $lPAG^{vGlut2}$ PRV+ neurons does not receive direct input (Figure 1N), suggesting that further processing may occur at the local level. Further experiments using high-density probes to perform *in vivo* recordings from a large population of neurons simultaneously will likely yield important insights about the local lPAG dynamics during aggression transformation.

Finally, the lPAG is only one of many outputs from the VMHvl. Recent reports show at least 25 outputs from the esr1+ VMHvl subpopulation alone (Lo et al., 2019). Therefore, the lPAG may represent only one piece of the VMHvl output circuit and may be involved solely in coordinating effector-specific motor components of aggression. The lPAG may generate action specificity by requiring coincident input from other nodes in the aggression circuit. Unlike stimulation-evoked attack from the VMHvl, which occurs in a time-locked and robust manner by recruiting a host of arousal and endocrinological mechanisms in addition to putative motor control populations, we found that our ability to evoke attack through the VMHvl-PAG pathway was generally unreliable. We reasoned that a more nuanced "on-manifold" activation pattern may be required to drive complex action. One likely candidate region (although there are many) that may provide coincident input is the dorsal medial PAG, which also receives excitatory input from the VMHvl and projects monosynaptically to the lPAG (Jansen et al., 1998). This projection could potentially behave as a second information loop in the hypothalamic-midbrain hierarchy.

Last, our functional inactivation experiments that specifically target $lPAG^{vglut2}$ neurons show a highly specific effect on the duration of attack (as opposed to the latency or number of behavioral episodes). Because attack latency is often used as a proxy for "escalated" or pathological aggression (Miczek et al., 2013), this suggests that the animal's overall state is not affected through inactivation and that the effects may be more motor in nature. This strongly indicates that the role of the lPAG in the aggression circuit is to coordinate the activity of multiple muscle groups rather than having a more general effect on the aggressive state. We liken the relationship between the hypothalamus and the PAG to execution of a piano sonata, where the activity in the VMHvl provides the song and the lPAG represents the keys on the piano. The hypothalamus is able to specify the key of the song, set the mood, and determine which chords are played, whereas the PAG population determines how keys are pressed and depressed.

STAR★METHODS

Detailed methods are provided in the online version of this paper and include the following:

- KEY RESOURCES TABLE
- LEAD CONTACT AND MATERIALS AVAILABILITY
- EXPERIMENTAL MODEL AND SUBJECT DETAILS
  - Animals
- METHOD DETAILS
  - *In vitro* electrophysiological recordings
  - Behavior analysis and tracking
  - PRV injections
  - Optogenetic activation
  - Chemogenetic Inactivation
  - Extracellular recording of freely moving mice
  - Electrophysiology Analysis
  - EMG implantation and recording
  - EMG analysis
  - Time-varying linear regression model
- QUANTIFICATION AND STATISTICAL ANALYSIS
- DATA AND CODE AVAILABILITY

SUPPLEMENTAL INFORMATION

Supplemental Information can be found online at https://doi.org/10.1016/j.neuron.2020.02.014.

ACKNOWLEDGMENTS

The authors wish to thank L. Enquist for the gift of the PRV 152 and 614; A. Chow, N. Cuvelier, C. Heins, and K. Liu for assistance with video annotation; T. Akay for EMG guidance; A. Person, K. Hashikawa, M. Halassa, and M. Long for helpful discussions; A. Hu and S. Oline for technical support; and D. Blackman for graphics. This work was supported by the Brain & Behavior Research Foundation (to A.L.F.); the Alfred P. Sloan Foundation (to A.L.F.); NIMH R00MH109674 (to A.L.F.); the Irma T. Hirschl Trust (to D.L.); and NIMH R01MH101377, R21MH105774, and 1U19NS107616-01 (to D.L.).

AUTHOR CONTRIBUTIONS

A.L.F. designed and carried out *in vivo* physiology and photometry experiments, performed all analyses and modeling for these experiments, and wrote and edited the manuscript. D.W. conducted the slice physiology experiments, analyzed the data, and co-wrote the manuscript. A.S. assisted with the PRV tracing experiments. P.C., L.W.W., and I.C. performed the chemogenetic and pharmacological inactivation experiments. J.E.F. constructed microdrives associated with the *in vivo* physiology experiments. D.L. conceived the project, suggested experiments, analyzed data, and edited the manuscript.

DECLARATION OF INTERESTS

The authors declare no competing interests.

Received: March 18, 2019
Revised: December 20, 2019
Accepted: February 10, 2020
Published: March 11, 2020

REFERENCES

Adams, D.B. (1968). Cells related to fighting behavior recorded from midbrain central gray neuropil of cat. Science *159*, 894–896.

Bandler, R., and Keay, K.A. (1996). Columnar organization in the midbrain periaqueductal gray and the integration of emotional expression. Prog. Brain Res. *107*, 285–300.

Bandler, R., and Shipley, M.T. (1994). Columnar organization in the midbrain periaqueductal gray: modules for emotional expression? Trends Neurosci. *17*, 379–389.

Chen, T.W., Wardill, T.J., Sun, Y., Pulver, S.R., Renninger, S.L., Baohan, A., Schreiter, E.R., Kerr, R.A., Orger, M.B., Jayaraman, V., et al. (2013). Ultrasensitive fluorescent proteins for imaging neuronal activity. Nature *499*, 295–300.

Davidson, A.G., O'Dell, R., Chan, V., and Schieber, M.H. (2007). Comparing effects in spike-triggered averages of rectified EMG across different behaviors. J. Neurosci. Methods *163*, 283–294.

Evans, D.A., Stempel, A.V., Vale, R., Ruehle, S., Lefler, Y., and Branco, T. (2018). A synaptic threshold mechanism for computing escape decisions. Nature *558*, 590–594.

Falkner, A.L., Dollar, P., Perona, P., Anderson, D.J., and Lin, D. (2014). Decoding ventromedial hypothalamic neural activity during male mouse aggression. J. Neurosci. *34*, 5971–5984.

Falkner, A.L., Grosenick, L., Davidson, T.J., Deisseroth, K., and Lin, D. (2016). Hypothalamic control of male aggression-seeking behavior. Nat. Neurosci. *19*, 596–604.

Fang, Y.Y., Yamaguchi, T., Song, S.C., Tritsch, N.X., and Lin, D. (2018). A Hypothalamic Midbrain Pathway Essential for Driving Maternal Behaviors. Neuron *98*, 192–207.e10.

Fay, R.A., and Norgren, R. (1997). Identification of rat brainstem multisynaptic connections to the oral motor nuclei using pseudorabies virus. I. Masticatory muscle motor systems. Brain Res. Brain Res. Rev. *25*, 255–275.

Fernandez De Molina, A., and Hunsperger, R.W. (1962). Organization of the subcortical system governing defence and flight reactions in the cat. J. Physiol. *160*, 200–213.

Franklin, T.B., Silva, B.A., Perova, Z., Marrone, L., Masferrer, M.E., Zhan, Y., Kaplan, A., Greetham, L., Verrechia, V., Halman, A., et al. (2017). Prefrontal cortical control of a brainstem social behavior circuit. Nat. Neurosci. *20*, 260–270.

Friard, O., and Gamba, M. (2016). BORIS: A Free, Versatile Open-Source Event-Logging Software for Video/audio Coding and Live Observations. Methods in Ecology and Evolution *7*, 1325–1330.

Gao, Z.R., Chen, W.Z., Liu, M.Z., Chen, X.J., Wan, L., Zhang, X.Y., Yuan, L., et al. (2019). Tac1-Expressing Neurons in the Periaqueductal Gray Facilitate the Itch-Scratching Cycle via Descending Regulation. Neuron *101*, 45–59.e9.

Gregg, T.R., and Siegel, A. (2001). Brain structures and neurotransmitters regulating aggression in cats: implications for human aggression. Prog. Neuropsychopharmacol. Biol. Psychiatry *25*, 91–140.

Gregg, T.R., and Siegel, A. (2003). Differential effects of NK1 receptors in the midbrain periaqueductal gray upon defensive rage and predatory attack in the cat. Brain Res. *994*, 55–66.

Hashikawa, K., Hashikawa, Y., Tremblay, R., Zhang, J., Feng, J.E., Sabol, A., Piper, W.T., Lee, H., Rudy, B., and Lin, D. (2017). Esr1^{+} cells in the ventromedial hypothalamus control female aggression. Nat. Neurosci. *20*, 1580–1590.

Holstege, G. (2014). The periaqueductal gray controls brainstem emotional motor systems including respiration. Prog. Brain Res. *209*, 379–405.

Jansen, A.S., Farkas, E., Mac Sams, J., and Loewy, A.D. (1998). Local connections between the columns of the periaqueductal gray matter: a case for intrinsic neuromodulation. Brain Res. *784*, 329–336.

Kittelberger, J.M., Land, B.R., and Bass, A.H. (2006). Midbrain periaqueductal gray and vocal patterning in a teleost fish. J. Neurophysiol. *96*, 71–85.

Klapoetke, N.C., Murata, Y., Kim, S.S., Pulver, S.R., Birdsey-Benson, A., Cho, Y.K., Morimoto, T.K., Chuong, A.S., Carpenter, E.J., Tian, Z., et al. (2014). Independent optical excitation of distinct neural populations. Nat. Methods *11*, 338–346.

Koutsikou, S., Apps, R., and Lumb, B.M. (2017). Top down control of spinal sensorimotor circuits essential for survival. J. Physiol. *595*, 4151–4158.

Lee, H., Kim, D.W., Remedios, R., Anthony, T.E., Chang, A., Madisen, L., Zeng, H., and Anderson, D.J. (2014). Scalable control of mounting and attack by Esr1+ neurons in the ventromedial hypothalamus. Nature *509*, 627–632.

Li, Y., Zeng, J., Zhang, J., Yue, C., Zhong, W., Liu, Z., Feng, Q., and Luo, M. (2018). Hypothalamic Circuits for Predation and Evasion. Neuron *97*, 911–924.e5.

Lin, D., Boyle, M.P., Dollar, P., Lee, H., Lein, E.S., Perona, P., and Anderson, D.J. (2011). Functional identification of an aggression locus in the mouse hypothalamus. Nature *470*, 221–226.

Lo, L., Yao, S., Kim, D.W., Cetin, A., Harris, J., Zeng, H., Anderson, D.J., and Weissbourd, B. (2019). Connectional architecture of a mouse hypothalamic circuit node controlling social behavior. Proc. Natl. Acad. Sci. USA *116*, 7503–7512.

Mathis, A., Mamidanna, P., Cury, K.M., Abe, T., Murthy, V.N., Mathis, M.W., and Bethge, M. (2018). DeepLabCut: markerless pose estimation of user-defined body parts with deep learning. Nat. Neurosci. *21*, 1281–1289.

Miczek, K.A., de Boer, S.F., and Haller, J. (2013). Excessive aggression as model of violence: a critical evaluation of current preclinical methods. Psychopharmacology (Berl.) *226*, 445–458.

Mos, J., Kruk, M.R., Van der Poel, A.M., and Meelis, W. (1982). Aggressive Behavior Induced by Electrical Stimulation in the Midbrain Central Gray of Male Rats. Aggress. Behav. *8*, 261–284.

Remedios, R., Kennedy, A., Zelikowsky, M., Grewe, B.F., Schnitzer, M.J., and Anderson, D.J. (2017). Social behaviour shapes hypothalamic neural ensemble representations of conspecific sex. Nature *550*, 388–392.

Schilling, D.L. (1991). Elements of Information Theory (John Wiley and Sons).

Schreiner, L., and Kling, A. (1953). Behavioral changes following rhinencephalic injury in cat. J. Neurophysiol. *16*, 643–659.

Shannon, C.E., and Weaver, W. (1964). The Mathematical Theory of Communication (University of Illinois Press).

Shimogawa, Y., Sakuma, Y., and Yamanouchi, K. (2015). Efferent and afferent connections of the ventromedial hypothalamic nucleus determined by neural tracer analysis: implications for lordosis regulation in female rats. Neurosci. Res. *91*, 19–33.

Siegel, A., Schubert, K.L., and Shaikh, M.B. (1997). Neurotransmitters regulating defensive rage behavior in the cat. Neurosci. Biobehav. Rev. *21*, 733–742.

Silva, C., and McNaughton, N. (2019). Are periaqueductal gray and dorsal raphe the foundation of appetitive and aversive control? A comprehensive review. Prog. Neurobiol. *177*, 33–72.

Smith, B.N., Banfield, B.W., Smeraski, C.A., Wilcox, C.L., Dudek, F.E., Enquist, L.W., and Pickard, G.E. (2000). Pseudorabies virus expressing enhanced green fluorescent protein: A tool for in vitro electrophysiological analysis of transsynaptically labeled neurons in identified central nervous system circuits. Proc. Natl. Acad. Sci. USA *97*, 9264–9269.

Srivastava, K.H., Holmes, C.M., Vellema, M., Pack, A.R., Elemans, C.P.H., Nemenman, I., and Sober, S.J. (2017). Motor control by precisely timed spike patterns. Proc. Natl. Acad. Sci. USA *114*, 1171–1176.

Stanek, E., 4th, Cheng, S., Takatoh, J., Han, B.X., and Wang, F. (2014). Monosynaptic premotor circuit tracing reveals neural substrates for oro-motor coordination. eLife *3*, e02511.

Timme, N.M., and Lapish, C. (2018). A Tutorial for Information Theory in Neuroscience. eNeuro *5*, ENEURO.0052-18.2018.

Tschida, K., Michael, V., Takatoh, J., Han, B.X., Zhao, S., Sakurai, K., Mooney, R., and Wang, F. (2019). A Specialized Neural Circuit Gates Social Vocalizations in the Mouse. Neuron *103*, 459–472.e4.

Wang, L., Chen, I.Z., and Lin, D. (2015). Collateral pathways from the ventromedial hypothalamus mediate defensive behaviors. Neuron *85*, 1344–1358.

Wang, L., Talwar, V., Osakada, T., Kuang, A., Guo, Z., Yamaguchi, T., and Lin, D. (2019). Hypothalamic Control of Conspecific Self-Defense. Cell Reports *26*, 1747–1758.e5.

Yang, C.F., Chiang, M.C., Gray, D.C., Prabhakaran, M., Alvarado, M., Juntti, S.A., Unger, E.K., Wells, J.A., and Shah, N.M. (2013). Sexually dimorphic neurons in the ventromedial hypothalamus govern mating in both sexes and aggression in males. Cell *153*, 896–909.

Zalcman, S.S., and Siegel, A. (2006). The neurobiology of aggression and rage: role of cytokines. Brain Behav. Immun. *20*, 507–514.

STAR★METHODS

KEY RESOURCES TABLE

REAGENT or RESOURCE	SOURCE	IDENTIFIER
Bacterial and Virus Strains		
AAV2-hSyn-DIO-hM4Di-mChery	Gift from Bryan Roth	Addgene viral prep # 44362-AAV2
AAV2.EF1a-DIO-hChR2(H134R)-EYFP	Gift from Karl Deisseroth	Addgene viral prep: 20298 Lot# v52304
AAV2-EF1a-double floxed-hChR2 (H134R)-mCherry-WPRE-HGHpA	Gift from Karl Deisseroth	Addgene viral prep # 20297-AAV1) Lot# AV4375H
AAV2/Ef1a-DIO-mCherry	Gift from Bryan Roth	UNC GTC Vector Core Prep
rAAV2.syn.flex.ChrimsonR.tdT	Gift from Ed Boyden; Klapoetke et al., 2014	UNC Vector Core prep: Lot # AV6555B
Pseudorabies virus (PRV) 152	Gift from Lynn Enquist; Smith et al., 2000	N/A
Pseudorabies virus (PRV) 614	Gift from Lynn Enquist; Smith et al., 2000	N/A
AAV1.CAG.Flex.GCaMP6f.WPRE.SV40	Gift from Douglas Kim and GENIE project; Chen et al., 2013	UPenn Vector Core: Lot # CS0956, CS0845, CS0224WL
HSV-Ef1a-LS1L-GCaMP6f	MIT Vector Core	Lot RN506
Chemicals, Peptides, and Recombinant Proteins		
tetrodotoxin	Alomone Labs	T-550; CAS: 18660-81-6
4-aminopyridine	Sigma-Aldrich	275875; CAS: 504-24-5
QX-314 chloride	Tocris	2313; CAS: 5369-03-9
DAPI	Life Technologies	D21490
CNO	Sigma	Cat#C0832
Mounting Medium	Vectashield	Cat#H1000
Experimental Models: Organisms/Strains		
Swiss Webster Wildtype mouse	Taconic	Tac: SW
BALB/c wildtype mouse	Taconic	Balb/cAnNTac
Mouse: Slc17a6$^{tm2(cre)Lowl}$ (vglut2-ires-cre)	The Jackson Laboratory	JAX: 028863
Mouse: Gt(ROSA)26 Sor$^{tm6(CAG-ZsGreen1)Hze}$ (Ai6 RCL-ZsGreen)	The Jackson Laboratory	JAX: 007906
Software and Algorithms		
DeepLabCut	Mathis et al., 2018	https://github.com/AlexEMG/DeepLabCut
BORIS	Friard and Gamba, 2016	https://www.boris.unito.it/
CalTech behaviorAnnotator	Lin et al., 2011	https://github.com/pdollar/toolbox
Offline Sorter	Plexon	https://plexon.com/products/offline-sorter/
StreamPix 5	NorPix	https://www.norpix.com/products/streampix/streampix.php
SpinView	FLIR	https://www.flir.com/products/spinnaker-sdk/
ClampEx 11.0 Digidata	Axon Instruments	https://www.moleculardevices.com/products/axon-patch-clamp-system/acquisition-and-analysis-software/pclamp-software-suite#RelatedProducts
MATLAB (Custom Code)	Available upon reasonable request	
Other		
Nanojector		N/A
400 μm multimode optic fibers	World Precision Instruments	Cat# Nanoliter 2000
230 μm multimode optic fibers	Thorlabs	Cat# BFH48-400
LED light	Thorlabs	Cat# TS1450308
LED driver	Thorlabs	Cat# M470F1

(*Continued on next page*)

Continued

REAGENT or RESOURCE	SOURCE	IDENTIFIER
Bandpass filter	Thorlabs	Cat# LEDD1B
Adjustable zooming lens	Semrock	Cat# FF02-472/30-25, FF01-535/505
Femtowatt silicon photoreceiver	Thorlabs, Edmund Optics	Cat# SM1NR01, #62-561
Real-time processor RP5 and RX8	Newport	Cat# 2151
13 mm tungsten microwires	TDT	RP5/RX8
Multi stranded wire for EMG	California Fine Wire	Cat# 100211
omnetics nano-connector	A-M Systems	Cat# 793200
Feedback-controlled commutator	Omnetics	Cat# A79014-001
16-channel preamplifier	TDT	Cat# ACO32
	TDT	Cat# RA16PA

LEAD CONTACT AND MATERIALS AVAILABILITY

- Further information about resources, reagents used, and requests for code should be directed to and will be fulfilled by the Lead Contact, Annegret Falkner (afalkner@princeton.edu).
- This study did not generate new unique reagents.

EXPERIMENTAL MODEL AND SUBJECT DETAILS

Animals

Experimental mice for recording, perturbation and behavior were sexually experienced, wild-type male C57BL/6N (12–24 weeks, Charles River), wild-type male Swiss Webster (12–24 weeks, Taconic), or *vGlut2*-ires-Cre mice. Sexually naive vGlut2 x Ai6 mice were used for slice physiology and tracing experiments. Intruders used for social interaction tests were group housed, sexually inexperienced BALB/c males, castrated group housed BALB/c males, or group housed C57BL/6 females (both 10–30 weeks). Mice were maintained on a reversed 12-h light/dark cycle (dark cycle starts at noon) and given food and water *ad libitum*. All experiments were performed in the dark cycle of the animals. All procedures were approved by the IACUC of NYULMC and Princeton University in compliance with the NIH guidelines for the care and use of laboratory animals.

METHOD DETAILS

In vitro electrophysiological recordings

vGlut2:Cre x Ai6 mice were injected with 100 nL rAAV2.syn.flex.ChrimsonR.tdT into VMHvl. Three weeks after virus injection, acute horizontal brain slices of VMHvl and PAG (275 μm in thickness) were collected using standard methods (Fang et al., 2018). After being anesthetized by isoflurane inhalation, the mice were perfused by ice-cold choline based cutting solution containing (in mM) 25 $NaHCO_3$,25 glucose, 1.25 NaH_2PO_4, 7 $MgCl_2$, 2.5 KCl, 0.5 $CaCl_2$, 110 choline chloride, 11.6 ascorbic acid, and 3.1 pyruvic acid. The slices were collected in the same cutting solution using a Leica VT1200s vibratome, incubated for 20 min in oxygenated artificial cerebrospinal fluid (ACSF) solution (in mM: 125 NaCl, 2.5 KCl, 1.25 NaH_2PO_4, 25 $NaHCO_3$, 1 $MgCl_2$, 2 $CaCl_2$ and 11 glucose) (osmolality, 295 mmol/kg) at 32– 34°C and then maintained at room temperature until use. Standard whole cell recordings were performed with MultiClamp 700B amplifier (Molecular Devices) and Clampex 11.0 software (Axon Instruments). Membrane currents were low-pass filtered at 2 kHz and digitized at 10 kHz with Digidata 1550B (Axon Instruments). Electrode resistances were 2–4 MΩ, and most neurons had series resistance from 4 to 15 MΩ. Glutamatergic (green fluorescent) or GABAergic (non-fluorescent) cells as well as Chrimson-tdTomato expressed VMHvl cells were identified with an Olympus 40 x water-immersion objective with GFP and TXRED filters. The slices were superfused with ACSF warmed to 32– 34°C and bubbled with 95% O_2 and 5% CO_2. The intracellular solutions for voltage clamp recording contained (in mM) 135 $CsMeSO_3$, 10 HEPES, 1 EGTA, 3.3 QX-314 (Cl– salt), 4 Mg-ATP, 0.3 Na-GTP, and 8 Na_2-Phosphocreatine (osmolality, 295 mmol/kg; pH 7.3 adjusted with CsOH), and for current clamp recording contained (in mM) 130 K $MeSO_3$, 5 KCl, 0.5 EGTA, 20 HEPES, 1.8 $MgCl_2$, 0.1 $CaCl_2$, 4 Na_2-ATP, and 0.2 Na-GTP (osmolality, 295 mmol/kg; pH 7.3 adjusted with KOH). To activate Chrimson-expressing VMHvl glutamatergic neurons and Chrimson-expression axons in PAG, brief pulses of full field illumination (20 ms for VMHvl during current clamp recording and 1 ms duration for PAG during voltage clamp recording) were delivered onto the recorded neuron with 605 nm LED light (pE-300white; CoolLED) at 35 s intervals. Voltage clamp recording was conducted for PAG neurons, and the membrane voltage was held at −70 mV for EPSC recording, and at 0 mV for IPSC recording. Current clamp recording was conducted in VMHvl glutamatergic neurons expressing Chrimson-tdTomato, where the neurons were maintained at resting potential and spiking activity was detected with or without red light pulses (20 ms, 20 Hz for 500 ms). For recordings of cells labeled with PRV, PRV-614 was injected to jaw muscle three weeks after

rAAV2.syn.flex.ChrimsonR.tdT injection into VMHvl of vGlut2:Cre x Ai6 mice. 96 hours after PRV injection, acute horizontal brain slices of PAG were collected for whole cell recordings.

Behavior analysis and tracking

All freely moving behaviors were recorded using top and side GigE cameras using StreamPix (Norpix) or Spinview (FLIR) and all videos were manually annotated for pre-identified behaviors and tracked for positional and velocity information using custom MATLAB Software (https://github.com/pdollar/toolbox), the Behavioral Observation Research Interaction Software (BORIS, https://www.boris.unito.it/) and DeepLabCut (Mathis et al., 2018). Behaviors were manually classified as previously described (Falkner et al., 2014); individual behaviors included attack, investigation of males, investigation of females, mounting, eating, and grooming. All social interactions were variants of the ''resident intruder assay'' (5-10 minutes of free interaction with male or female intruder), or alternating interactions with males and females (1 min each) separated by 1 min (Figure 5) in the home cage of the experimental animal.

PRV injections

The right masseter was exposed and PRV-152 or PRV-614 (kind gift from Lynn Enquist), was injected at 5 separate locations, 250uL per injection along the A-P axis of the muscle. The skin was sutured closed and PRV was incubated for 96-112 hours prior to sacrifice. For vGlut2 Ai6 overlap experiments, PRV labeled neurons in PAG were counted on sequential 50uM thick sections through the PAG. A total of 9 sections were counted across 3 animals.

Optogenetic activation

For optogenetic activation experiments we injected wild-type males with a 2:1 mixture of 100-150nl of AAV2-CMV-Cre (2 × 1012 PFU/ml) and AAV2.EF1a-DIO-hChR2(H134R)-EYFP (1 × 1012 PFU/ml, both from UNC vector core) ipsilaterally in the VMHvl (−1.82A/P, 0.72M/L, −5.8D/V) and a 230-μm multimode optic fiber (Thorlabs) was positioned 0.5mm over the injection site and over the terminal field in the lPAG targeting the middle third of the column (coordinates: −4.29 A-P, +/−0.45 M-L, −1.9 D-V). vGlut2-ires-cre males were injected with 130nl of AAV-EF1a-double floxed-hChR2(H134R)-mCherry-WPRE-HGHpA (Addgene 20297, 1.8 × 10^13, Lot V31400). Optogenetic testing on the cell bodies was performed 3 weeks following viral injection. The other end of the optic fiber was connected to a 473-nm laser (Shanghai Dream Lasers or Opto Engine) controlled by computer-programmed TTL pulses. For optogenetic activation, animals were screened for 'functional' injection sites using a resident-intruder test to determine whether stimulation of each injection site was sufficient to evoke attack of a castrated BALB/c male. High frequency (10–20 Hz, 10-ms pulses, 0.5–1.5 mW) stimulation was delivered through the optic fiber for 20–30 s, with a minimum duration of 30 s between stimulation trials. Stimulated animals received 5–10 stimulation trials during each test session for each injection site (∼15 min). Consistent with our previous report, light activation of functionally defined sites caused animal to orient toward, approach, investigate, and eventually attack the intruder. If animals showed robust attack during this test (attack within 30 s of stimulation on, on > = 50% of trials), they were used for the terminal stimulation experiments.

Chemogenetic Inactivation

For reversible inactivation with DREADD gi, we stereotactically injected vGlut2-ire-cre mice with 100nl of AAV2-hSyn-DIO-hM4Di-mChery (Addgene, 44362-AAAV2, titer: 1.4 × 10^13 pfu/ml, Lot v30430) bilaterally in the lPAG at 3 sites along the A-P column of the PAG (coordinates: −3.93 A-P, +/−0.30 M-L, −2.3 D-V;-4.29 A-P, +/−0.45 M-L, −2.3 D-V; −4.75 A-P, +/−0.45 M-L, −2.3 D-V;).

Control animals were injected with AAV2/Ef1a-DIO-mCherry (UNC GTC Vector Core, titer: 5.3x10^12 pfu/ml, Lot: AV4375H). Three weeks following injections animals were tested for aggression on three consecutive days. If levels of aggression had stabilized, animals were injected with either 1mg/kg CNO or the equivalent amount of saline i,p., then after 30 minutes, were presented with a male for 5 minutes followed by a 2 minute break, then a female for 5 minutes followed by a two minute break. Animals were then given a yogurt chip and allowed to approach and consume the food. Behaviors were compared between the saline and CNO injection days for both groups of animals.

Extracellular recording of freely moving mice

Methods for physiological recording in freely moving animals were described previously (Lin et al., 2011; Falkner et al., 2014). Custom-built 16-channel (or 14 channel with EMG) tungsten electrode bundles or groups of tetrodes were attached to a moveable microdrive and implanted over the lPAG. After allowing 2 weeks for recovery, we connected the implanted electrode to a 16-channel headstage. Signals were streamed into a commercial acquisition system through a torqueless, feedback-controlled commutator (Tucker Davis Technology) and band-pass filtered between 100 and 5,000 Hz. Digital infrared videos of animal behavior from both side- and top-view cameras were simultaneously recorded at 640 × 480 pixel resolution at 25 frames per second (Streampix, Norpix). Video frame acquisition was triggered by a TTL pulse from the acquisition system to achieve synchronization between the video and the electrophysiological recording. Spikes were sorted manually using commercial software (OfflineSorter, Plexon) based on principal component analysis. Unit isolation was verified using autocorrelation histograms. To consider the recorded cell as a single unit, cells had to have a signal/noise ratio > 2; spike shape had to be stable throughout the recording; and the percentage of spikes occurring with inter-spike intervals (ISIs) < 3 ms (the typical refractory period for a neuron) in a continuous recording sequence had to

be < 0.1%. We checked for redundancies within days by examining the cross correlations of co-recorded neurons and checked for redundancies across days by comparing waveforms and temporal response profiles. After the first recording, the implanted electrode was slowly moved down in 40-μm increments. The placement of the electrode was examined histologically with the aid of DiI coated on the electrodes. Animals were excluded if electrodes were not confined to the PAG. Recordings of the VMHvl (Figures 3F–3J) were performed previously using identical methods (Falkner et al., 2014; Lin et al., 2011) and reanalyzed here for direct comparison to PAG neurons.

Electrophysiology Analysis

Spikes in single neurons were convolved with a 25 ms Gaussian for presentation (Figure 3D). Responsivity index (RI) for each behavior (Figures 3I and 3J) was computed as

$$RI = \frac{Activity_{Behavior} - Activity_{BaselineNonsocial}}{Activity_{Behavior} + Activity_{BaselineNonsocial}}$$

Where $Activity_{behavior}$ is defined as the mean activity across all episodes of a particular behavior (e.g., attack) and $Activity_{BaselineNonsocial}$ is defined as the mean activity across all episodes designated as non-social within the given social interaction. Within-neuron significance was determined using a paired t test for each neuron (behavior versus nonsocial) compared to a Bonferroni-corrected threshold for each tested population.

EMG implantation and recording

To perform simultaneous recordings of PAG neurons and jaw muscle activity, we implanted animals with chronic EMG electrodes in the right masseter superficial muscles of the jaw. Electrodes were constructed using a pair of 0.001 inch flexible multi-strand stainless steel wires (A-M Systems, No. 793200) with the insulation removed from a 0.5-mm segment of each wire such that pairs of electrodes recorded signals from separate but nearby areas of the same muscle. Electrode wires were threaded through the muscle during a surgical procedure and anchored with a knot on the outside of the muscle. EMG wires were then threaded under the skin to the base of the skull where they were attached to ground electrodes. EMG wire output was relayed through a preamplifier and commutator to the digitizer with a sampling rate of 3,000 Hz (Tucker Davis Technology). Signals were processed by taking the difference from the pair of electrodes, and this differential signal was low pass filtered at 300 Hz.

EMG analysis

Mutual Information

Mutual information was computed between simultaneously recorded PAG activity and jaw EMG. EMG signals were rectified, low pass filtered at 20Hz, and downsampled to 1kHz. Spike trains were converted into a continuous instantaneous firing rate (IFR) with the same number of points as the downsampled EMG signals. For each pair of recorded PAG instantaneous firing rate and EMG signal, the continuous signals were discretized and MI was computed according to the definition (Shannon and Weaver, 1964; Schilling, 1991; Timme and Lapish, 2018):

$$MI(X;Y) = \sum_{x,y} p_{XY}(x,y) \log \frac{P_{XY}(x,y)}{P_X(x)P_Y(y)} = E_{P_{xy}} \log \frac{P_{XY}}{P_X P_Y}$$

Where x and y represent the instantaneous firing rate and EMG signal respectively.

For each signal pair, the MI was compared relative to the mean of ten iterations of a circularly permuted time shuffled control.

Spike Triggered EMG

STEMGs were computed on rectified EMG signals by averaging the EMG signal in an 800ms window around each PAG spike recorded during interactions with a male or with a female. STEMGs were computed separately for each 10 s increment during male and female interactions, smoothed with a 5ms moving average, then normalized by the number of spikes. To correct for drift due to volleys of successive spikes, STEMGs were baseline corrected by subtracting a baseline 100ms boxcar filtered version of the STEMG. To determine whether STEMGs contained significant peaks, we set strict criteria: STEMGs had to have a minimum of 5 consecutive points that crossed above the 98% confidence interval within 60ms of the 0 (the spike onset).

Fiber photometry recordings

A rig for performing simultaneous fiber photometry recordings from 2 locations was constructed following basic specifications previously described with a few modifications. For simultaneous VMH and VMHvl-PAG recordings, we injected vGlut2-ires-cre males with 100-160nl of

AAV1.CAG.Flex.GCaMP6f.WPRE.SV40 (Lot CS0956, CS0845, CS0224WL, Upenn, final titer:: 9.3 × 10^12 PFU/ml) ipsilaterally into the VMHvl, and 240nl of HSV-Ef1a-LS1L-GCaMP6f (MIT vector core,Lot RN506, final titer: 1.0 × 10^9 PFU/ml) contralaterally in the PAG. For simultaneous recordings of the VMHvl and lPAG, we injected 80-120nl of AAV2/1 CAG::Flex-GCaMP6f-WPRE-SV40 ipsilaterally into the VMHvl, and 160-240nl of AAV2/1 CAG::Flex-GCaMP6f-WPRE-SV40 in the lPAG. VIruses were injected using the following coordinates: VMHvl (−1.82A/P, 0.72M/L, −5.8D/V), lPAG(−3.64A/P, 0.5M/L-2.4D/V).

A 400-μm optic fiber (Thorlabs, BFH48-400) housed in a metal ferrule (Thorlabs, SFLC440-10) was implanted 0.4 mm above each injection site, except for the HSV-Ef1a-LS1L-GCaMP6f injection, where the fiber was placed over the VMHvl. After three weeks of viral incubation and before recording, a matching optic fiber was connected to the each implanted fiber using a ferrule sleeve. A 400-Hz sinusoidal blue LED light (30-50 μW) (LED light: M470F1; LED driver: LEDD1B; both from Thorlabs) was bandpass filtered (passing band: 472 ± 15 nm, Semrock, FF02-472/30-25) and delivered to the brain to excite GCaMP6. The emission light then traveled through the same optic fiber, was bandpass filtered (passing band: 534 ± 25 nm, Semrock, FF01-535/50), detected by a femtowatt silicon photoreceiver (Newport, 2151) and recorded using a real-time processor (RZ5, TDT). The envelope of the 400-Hz signals that reflects the intensity of the GCaMP6 signals were extracted in real-time using a custom TDT program. Baseline adjusted fluorescence signals were regressed using a 30 s spline approximation.

Histology and imaging

Animals were deeply anaesthetized using 0.5 mL of a ketamine-xylazine cocktail (10 mg/ml ketamine and 5 mg/ml xylazine) and transcardially perfused with phosphate buffered saline (PBS) followed by cold 4% paraformaldehyde in PBS. Brains were immersed overnight in a 20% sucrose solution, embedded with cutting medium (Tissue-Tek) and sectioned using a cryostat (Leica). Standard immunohistochemistry procedures were followed to stain 30-μm coronal brain sections for all mice. DAPI (1:20,000, Life Technologies, catalog number D21490, widely validated) was used to assess electrode track for physiology and fiber track for photometry. We acquired 2.5x or 5x, fluorescent images to determine cannula or electrode placements amd 20x fluorescent images to determine viral expression. We used 10 × fluorescent images to count PRV+. Cell counting in synaptophysin-injected animals was done manually using ImageJ on 30-μm sections separated by 60 μm that had observed GFP label in the lPAG.

Time-varying linear regression model

We modeled the population response of the PAG during male and female interactions for each animal by fitting the PAG response during each interaction including 10 s prior to the introduction and 10 s following the removal of the animals with a series of autoregressive models using time-varying lengths of simultaneously recorded VMHvl signal as the variable regressors using the form:

$$PAG(t) = \beta_0 + \beta_1 VMH(t) + \beta_2 VMH(t-1) + \beta_3 VMH(t-2) + \ldots \beta_n VMH(t-n)$$

where t represents the current time bin and the other regressors represent variable amounts of elapsed time. PAG and VMHvl signals were binned in either 50ms, 100ms, 250ms, 500ms, and 1 s bins and models were fit independently for each of these bin sizes. For each VMHvl and PAG signal, data was halved and the first half was used to fit and the second half was used to cross validate, using least-squares. Model order was set to maximum value of 10 s of elapsed time, set independently for each bin size. For each family of models fit to the data, the best order model was determined using AIC (Akaike Information Criteria) on the fit to the cross validated data. A timeshifted null model was fit by circularly permuting the input data (VMHvl) signal and fitting the unpermuted PAG signal, and fit and model order were re-fit for the timeshifted data. Model order for the selected model was converted to elapsed time for each binsize. Fits were performed separately for male and female interactions. Additionally, we tested the alternative hypothesis that PAG signals influence VMHvl signal by fitting the "reverse" model of the form:

$$VMH(t) = \beta_0 + \beta_1 PAG(t) + \beta_2 PAG(t-1) + \beta_3 PAG(t-2) + \ldots \beta_n PAG(t-n)$$

A similar model family was fit for the reverse model, and the model order (and elapsed time) was determined for each model independently for each bin size.

QUANTIFICATION AND STATISTICAL ANALYSIS

All statistical analysis was performed using MATLAB. Parametric tests, including Student's t test, paired t test, and two-sample t test were used if distributions passed Kolmogorov–Smirnov tests for normality. For within-neuron tests of firing rate significance, a nonparametric Wilcoxon signed rank test was used since spike rates were often low and not normally distributed. Repeated tests of significance were corrected with a strict Bonferroni correction. For all statistical tests, significance was measured against an alpha value of 0.05 unless otherwise stated. All error bars show s.e.m. No statistical methods were used to predetermine sample sizes, but our sample sizes are similar to those reported in previous publications. Data collection and analysis were not performed blind to the conditions of the experiments. Statistical detail can be found in the figure legends for individual figures and in some cases, reported in the results.

Statistical analyses used in each figure are listed below.

Figure 1. (I,Q) Paired t test
Figure 2. (C-J, L-M) Paired t test
Figure 3. (B) Single neuron activity average using 25ms Gaussian smoothing (C-E) Top panels are the z-scored responses of individual neurons aligned to each behavior, and histograms represent the number of neurons whose peak response lies at that bin relative to behavior onset. Dotted line represents chance level (number of bins/number of neurons). (G-H) Wilcoxon signed rank test for comparison of population response. Percentages of neurons in pie charts computed using within-neuron significance test

across one or both behaviors, with Bonferroni correction. (I) Kolmogorov-Smirnov test (J) Unpaired t test across all bins using Bonferroni corrected threshold across all bins.
Figure 4. (C) Kolmogorov-Smirnov test between cumulative distributions. (F-G) Significant EMGsm+ neurons see methods.
Figure 5. (D,E) Fisher's test, (D-G,) paired t test, (D-E,G) Error bars show ± SEM, comparisons of means with paired t test.
Figure 6. (D) paired t test (E) Error bars show ± SEM (F) Wilcoxon signed rank test of male, female, and baseline activity. (H-I) Paired t test between forward and null model at each bin for fit, Paired t test between male and female interactions for model time.
Figure S1. (C) Paired t test.
Figure S2. (D-E) Paired t test.
Figure S3. (C,H,M) Wilcoxon signed rank test on mean EMG 5 s pre compared to 5 s post behavior. (E,J,O) Wilcoxon signed rank test on mean activity 5 s pre compared to 5 s post behavior.
Figure S4. (A-B,D-E) Activity shown is z-scored across the whole interaction trace. (C,F) Activity for each individual behavior is baseline subtracted using a 1 s bin 5 s prior to interaction. Individual behaviors compared using student's ttest, and comparison between behaviors using an unpaired t test.

DATA AND CODE AVAILABILITY

All data and code are available upon reasonable request.

Neuron, Volume *106*

Supplemental Information

Hierarchical Representations of Aggression in a Hypothalamic-Midbrain Circuit

Annegret L. Falkner, Dongyu Wei, Anjeli Song, Li W. Watsek, Irene Chen, Patricia Chen, James E. Feng, and Dayu Lin

Supplementary Figure Legends

Figure S1. Related to Figure 1.

PRV-labeled jaw-projecting neurons are maximally within VMHvl$^{vGlut2+}$ projection-defined column boundaries and are aggression relevant. (A) Experimental procedure for determining overlap between VMHvl projection fields and PRV label. (B) Example histology showing VMHvl synaptophysin-containing terminals (left), PRV-GFP labeled jaw-projecting neurons (center), and overlap (right). (C) Number of GFP labeled neuron observed within each PAG column. N=4 animals, p=0.0028, one-way ANOVA (D) Putative circuit from excitatory vGlut2+ neurons to jaw.

Figure S2. Related to Figure 2.

Optogenetic activation of of VMH-PAG pathway can induce attack in some individuals with low efficacy. (A) Wild-type animals were injected at the VMHvl with a combination of ChR2 and cre, and vGlut2-ires-cre animals were injected with ChR2 at the VMHvl. Fibers were placed over the VMHvl and the lPAG. (B) Experimental animals were screened and excluded if ChR2 stimulation did not evoke time-locked attack of a castrated male from stimulation of the VMHvl on at least 50% of trials, and those non-excluded animals were tested through stimulation of the VMH-PAG projection during interaction with a castrated male. (C) All stimulation trials of wild-type animals (left), vGlut2-ires-cre animals (middle), and light only controls (right). (D) Stimulation significantly increased the probability of attack in the wildtype animals during the first 90s of stimulation (D, left, p=0.007, N=8 animals) but change was more variable in the vGlut2-ires-cre animals (D, middle, p=0.080, N=8 animals). No difference was observed in attack probability in controls (D, right, p=0.645, N=6 animals). (E) Activation of the VMHvl-PAG pathway did not significantly increase the percent time spent attacking in either the wildtype animals, (E, left, p=0.064), vglut2-ires-cre animals (E, middle p=0.565), or controls (E, right,

p=0.459), suggesting that activation of this pathway may be insufficient to drive robust and complete attack behavior. All comparisons done with paired t-test.

Figure S3. Related to Figure 4.

lPAG activity is not modulated during other jaw-dependent behaviors (A,F,K) Example rectified EMG signal during a single episode of attack (A), eating (F), and grooming (K). Shaded area shows time spent in behavior. Behavior-aligned EMG activity during neurons recorded simultaneously with EMG for attack (B), eat (G), and groom (L). Black trace shows rectified EMG mean +SEM. Mean rectified jaw EMG activity is increased during each of the three behaviors relative to a pre-behavior epoch (5s): attack (C, $p<0.0001$), eating (H, $p=0.00002$) and grooming (M, $p=0.0006$). Activity in co-recorded neurons during a similar epoch is only increased during attack (D-E, $p=0.002$), but is not significantly modulated during eating (I-J, $p=0.182$) or grooming (N-O, $p=0.406$). All pairwise comparisons done with Wilcoxon signed rank test on N=64 sessions with simultaneous EMG and lPAG neurons. Sorts of neural and EMG activity performed using descending attack aligned activity shown in D. Activity during eating is significantly decreased relative to attack (A, N=26, $p=0.0007$), and nonsocial epochs (B, N=26, $p=0.0006$). Gray dots represent single neurons tested in both behaviors. (C) Activity during grooming is decreased relative to nonsocial epochs (N=87, $p=0.004$). (D) Neurons with significant STEMG activity do not show activity increases aligned eating or grooming onsets, but do show activity aligned to attack. All pairwise comparisons done with Wilcoxon signed rank test.

Figure S4. Related to Figure 5.

Fiber photometry responses to individual male behaviors during simultaneous recordings. (A-B) PETHs comparing simultaneously recorded mean VMHvl (black) and VMHvl-lPAG (magenta)

aligned to attack (A) and investigate male (B) N=6 animals. (C) Comparison of individual behavior episodes for attack (red) and investigate male (blue). Both attack and investigate male acutely increase VMHvl and VMHvl-lPAG responses (***p=9.2157*10^-13, ***p=1.3144*10^-6, N=84 attack episodes in 6 animals; ***p=1.8445*10^-7, ***p=2.6243*10^-7, N=85 investigate male episodes in 6 animals, one sample ttest; Comparison between behaviors, VMHvl: ***p=5.157*10^-4, VMHvl-lPAG: p=0.4201). (D-E) PETHs comparing simultaneously recorded mean VMHvl (black) and lPAG (magenta) aligned to attack (D) and investigate male (E) N=7 animals. (F) Comparison of individual behavior episodes for attack (red) and investigate male (blue). Attack acutely increases VMHvl and lPAG (***p=2.9198*10^-11, ***p=4.0921*10^-5, N=84 attack episodes in 6 animals), but investigate only increases VMHvl (***p=2.1263*10^-5, p=0.5164, N=85 investigate male episodes in 7 animals, one sample ttest). Comparison between behaviors, VMHvl: ***p=5.157*10^-4, VMHvl-lPAG: p=0.4201). lPAG responses are significantly different between attack and investigate, while VMHvl responses are not (VMHvl: p=0.1467, lPAG: ***p=5.7677*10^-4, N=84 attack episodes, N=85 investigate male episodes in N=7 animals, unpaired ttest).

Figure S5. Related to Figure 6.

Injection maps of viral spread of AAV-FLEX-GCaMP6f for animals used for simultaneous VMHvl and lPAG recordings (Figure 6).

Figure S1

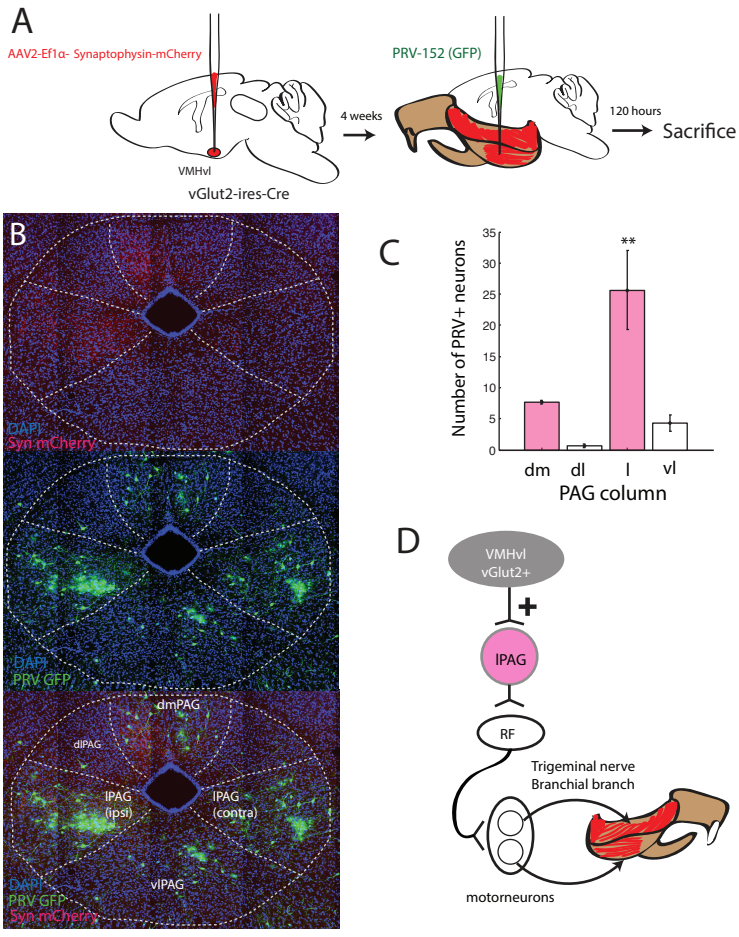
A
AAV2-Ef1α- Synaptophysin-mCherry
PRV-152 (GFP)
4 weeks
120 hours
Sacrifice
VMHvl
vGlut2-ires-Cre
B
DAPI
Syn-mCherry
DAPI
PRV GFP
dmPAG
dlPAG
lPAG
(ipsi)
lPAG
(contra)
vlPAG
DAPI
PRV GFP
Syn-mCherry
C
Number of PRV+ neurons
35
30
25
20
15
10
5
0
**
dm
dl
l
vl
PAG column
D
VMHvl
vGlut2+
+
lPAG
RF
Trigeminal nerve
Branchial branch
motorneurons

Figure S2

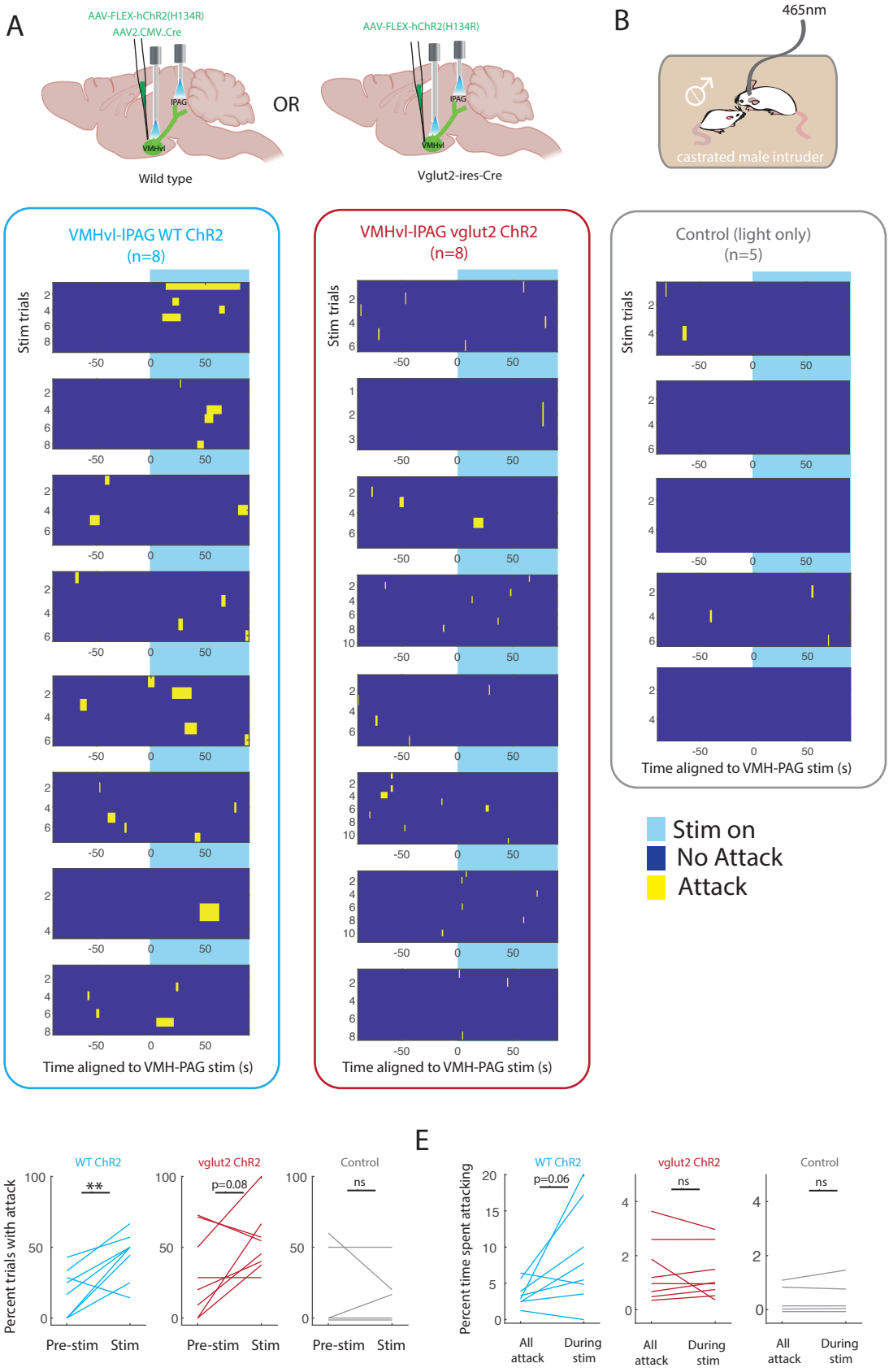
A
AAV-FLEX-hChR2(H134R)
AAV2.CMV..Cre
IPAG
VMHvl
Wild type
OR
AAV-FLEX-hChR2(H134R)
IPAG
VMHvl
Vglut2-ires-Cre
B
465nm
castrated male intruder
C
VMHvl-lPAG WT ChR2
(n=8)
Stim trials
Time aligned to VMH-PAG stim (s)
VMHvl-lPAG vglut2 ChR2
(n=8)
Stim trials
Time aligned to VMH-PAG stim (s)
Control (light only)
(n=5)
Stim trials
Time aligned to VMH-PAG stim (s)
Stim on
No Attack
Attack
D
WT ChR2
vglut2 ChR2
Control
Percent trials with attack
**
p=0.08
ns
Pre-stim
Stim
E
WT ChR2
vglut2 ChR2
Control
Percent time spent attacking
p=0.06
ns
ns
All attack
During stim

Figure S3

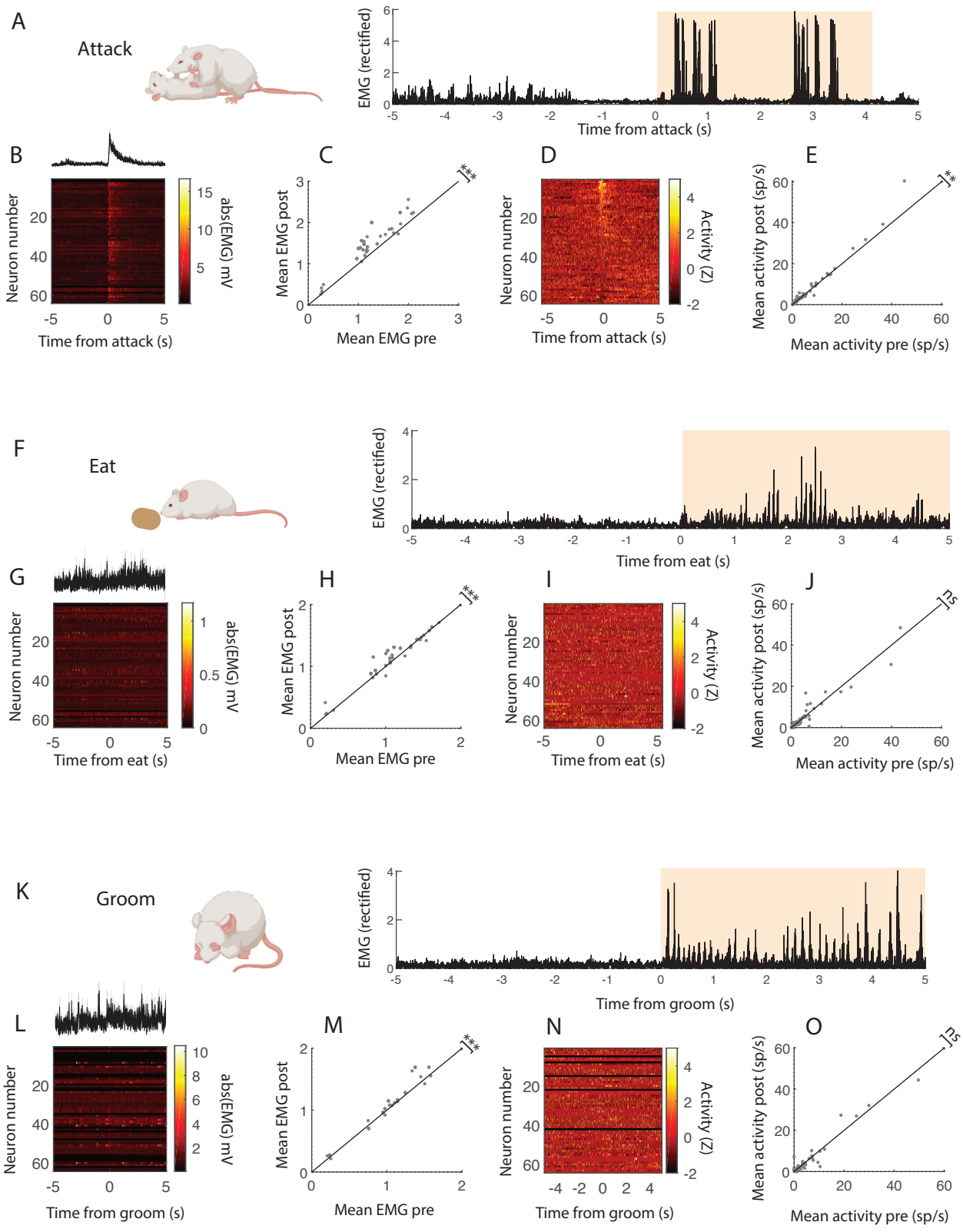
A
Attack
EMG (rectified)
Time from attack (s)
B
Neuron number
abs(EMG) mV
Time from attack (s)
C
Mean EMG post
Mean EMG pre
***
D
Neuron number
Activity (Z)
Time from attack (s)
E
Mean activity post (sp/s)
Mean activity pre (sp/s)
**
F
Eat
EMG (rectified)
Time from eat (s)
G
Neuron number
abs(EMG) mV
Time from eat (s)
H
Mean EMG post
Mean EMG pre
***
I
Neuron number
Activity (Z)
Time from eat (s)
J
Mean activity post (sp/s)
Mean activity pre (sp/s)
ns
K
Groom
EMG (rectified)
Time from groom (s)
L
Neuron number
abs(EMG) mV
Time from groom (s)
M
Mean EMG post
Mean EMG pre
***
N
Neuron number
Activity (Z)
Time from groom (s)
O
Mean activity post (sp/s)
Mean activity pre (sp/s)
ns

Figure S4

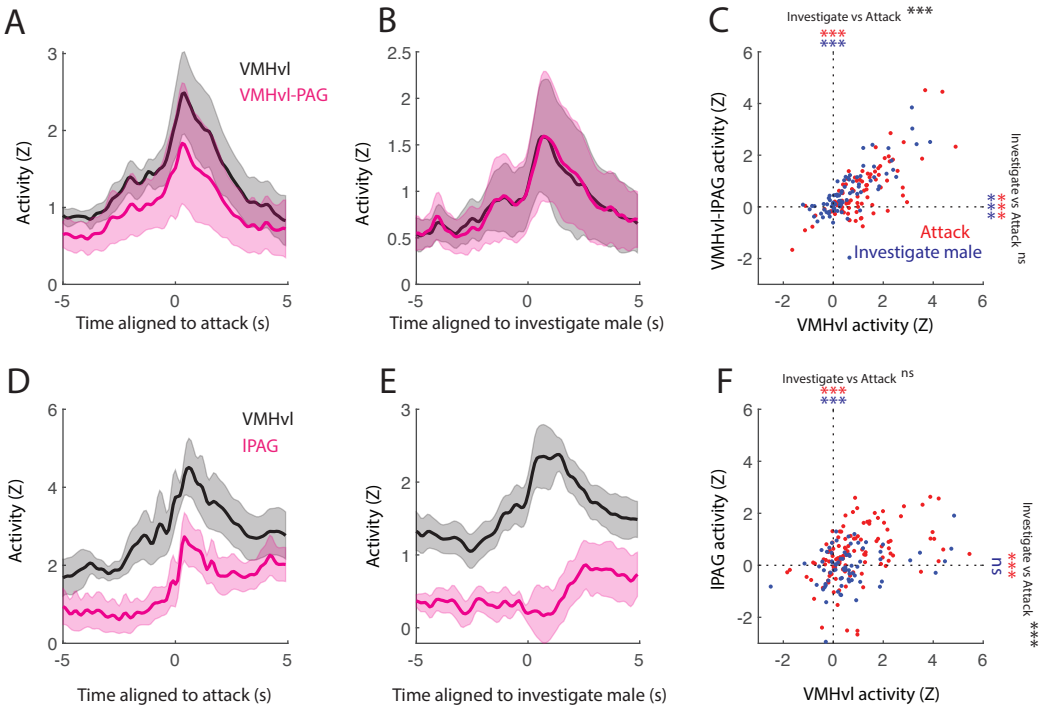
A
VMHvl
VMHvl-PAG
Activity (Z)
Time aligned to attack (s)
B
Activity (Z)
Time aligned to investigate male (s)
C
Investigate vs Attack ***
VMHvl-lPAG activity (Z)
VMHvl activity (Z)
Attack
Investigate male
Investigate vs Attack ns
D
VMHvl
lPAG
Activity (Z)
Time aligned to attack (s)
E
Activity (Z)
Time aligned to investigate male (s)
F
Investigate vs Attack ns
lPAG activity (Z)
VMHvl activity (Z)
Investigate vs Attack ***

Figure S5

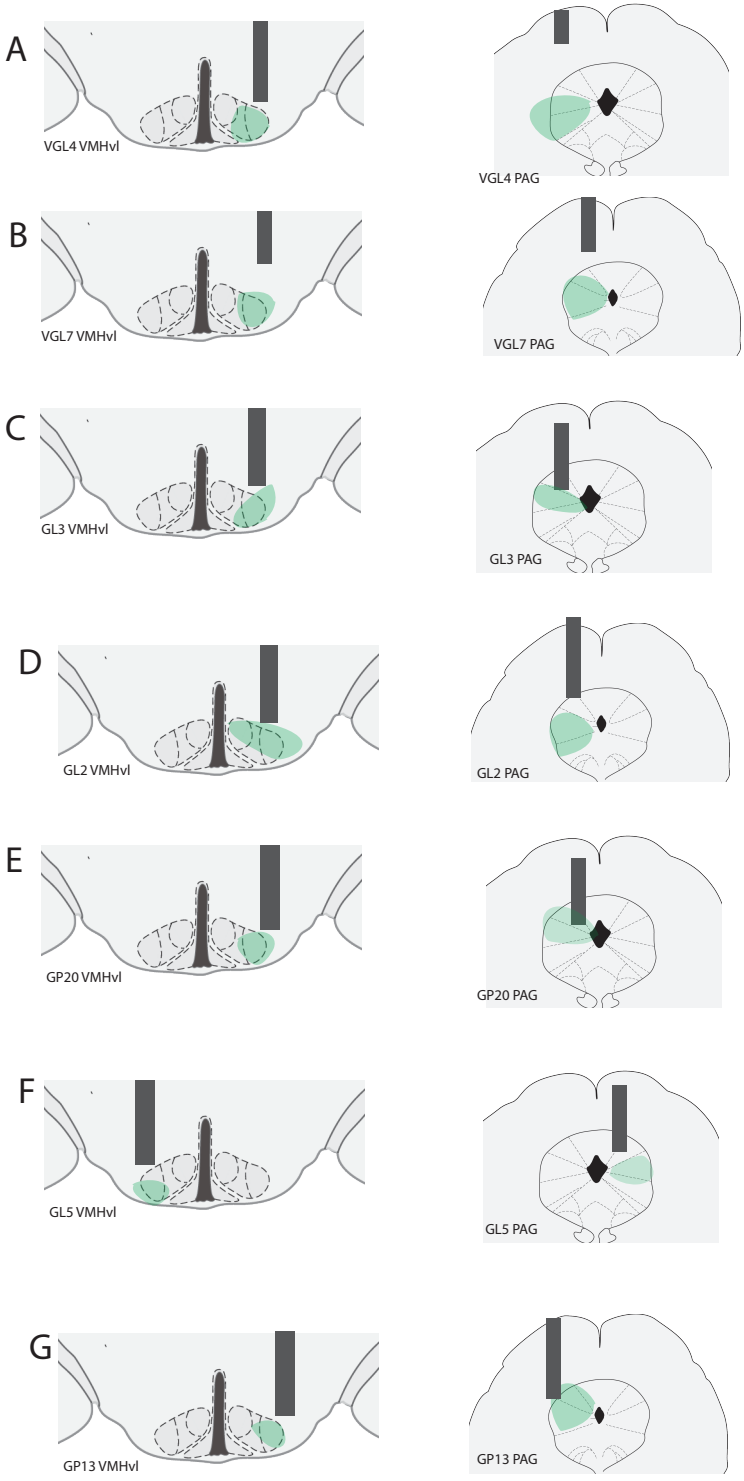
A
VGL4 VMHvl
VGL4 PAG
B
VGL7 VMHvl
VGL7 PAG
C
GL3 VMHvl
GL3 PAG
D
GL2 VMHvl
GL2 PAG
E
GP20 VMHvl
GP20 PAG
F
GL5 VMHvl
GL5 PAG
G
GP13 VMHvl
GP13 PAG